Investigating the source of the high nitrate, low oxygen layer in the Leeuwin Current

By

Meng Han

A thesis submitted in partial fulfilment of the requirements of the Bachelor of Marine and Antarctic Science with Honours

at the

Institute for Marine and Antarctic Studies (IMAS), University of Tasmania

July 2020

Declaration

I declare that all material in this thesis is my own work and contains no material that has been accepted for the award of any other degree or diploma in any tertiary institution and that, to be the best of my knowledge, contains no material previously published or written by another person, except where due reference is made in the text of this thesis.

韩萌

Meng Han

13rd July 2019

Abstract

The Leeuwin current (LC) is the only poleward flowing eastern boundary current in the world and has unique characteristics. In the absence of wind-driven upwelling against the coast, the shelf scale midwinter bloom is a mysterious feature. A high nitrate low dissolved oxygen (HNLDO) layer that has been observed in the LC is considered to be a possible source of nutrients to support the winter bloom. There is evidence to suggest that the Eastern Gyral Current (EGC) delivers the HNLDO layer into the LC. In this study, the water properties in the EGC have been sampled at fine resolution at several locations as the EGC approaches the coast. The HNLDO layer is observed between 100-150 m depth in observations from the undulating towed-body Triaxus and CTD profiles. The transport of the EGC across the tracks is also estimated and suggests that the active eddy field along the path of the EGC has a strong influence on the EGC structure and pathway. Since the HNLDO is observed in the EGC and the EGC feeds into the LC, we infer that the EGC transports the layer into the LC and southward along the west coast of Australia. The transport of volume, heat, salinity, oxygen and nitrate by the EGC can then be used to further study the HNLDO layer in the LC over a longer period.

Acknowledgement

First, I wish to express my sincere thanks to my brilliant supervisors Helen Phillips and Peter Thompson. They are always very patient and supportive and provide me lots of invaluable help through my honours year. I have learnt a lot from them.

I would also thank University of Tasmania and Institute for Marine and Antarctic Studies for the Honours 2+2 program in cooperation with Ocean University of China.

I would like to extend my gratitude to Fraser Kennedy for great proofreading of my writing. Thanks to my close friends, especially Kai Wang, Ziwei Zhang and Yuxin Wang. They support me and encourage me to finish the honours year successfully.

Last but not least, thanks to my family for their unwavering supporting as well as love for the long time. The life in UTAS is one of the most unforgettable experience in my life, I appreciate support from all people around me.

Table of Contents

Figure list

Table list

1 Introduction

1.1 Indian Ocean Circulations

In recent years, the Indian Ocean is considered to have had a significant impact on global climate change due to its unique circulation and monsoon system. Located at the northern boundary of the Indian Ocean is the Asian continent which drives strong monsoonal winds that generate seasonally variable currents in the Northern Indian Ocean (Schott, Xie & McCreary Jr 2009). As a result, the North Indian Ocean lacks the steady equatorial easterly winds present in the Pacific and Atlantic Oceans. These equatorial easterlies drive upwelling of nutrient rich water at the equator, which stimulates ocean productivity in these water masses. In contrast, the equatorial Indian Ocean is low in productivity.

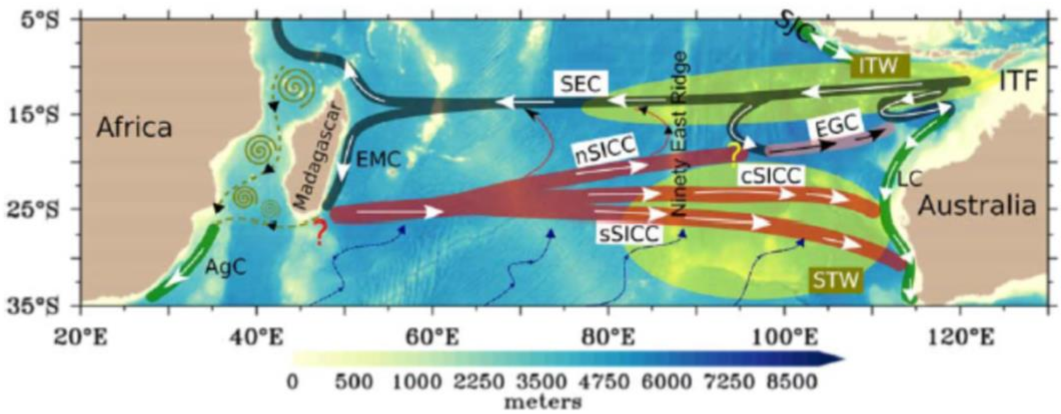

Figure 1. Surface circulation of the South Indian Ocean. Currents indicated are the three branches of the South Indian Countercurrent (northern [nSICC], central [cSICC], and southern [sSICC]), the South Equatorial Current (SEC), the East-Madagascar Current (EMC), Agulhas Current (AgC), the seasonally reversing South Java Current (SJC), the Eastern Gyral Current (EGC), and the Leeuwin Current (LC). Question marks (?) indicate regions where the circulations are still a matter of debate: the retroflection of the EMC and its connection to the SICC, and the connection between the SICC and the tropical EGC. Spirals indicate the southward-propagating Mozambique Channel eddies. Yellow shadings show the Indonesian Throughflow Water (ITW) and the subtropical Water (STW) regions. ITF stands for the Indonesian Throughflow. Water depths are blue shadings from the Smith-Sandwell 2 min bathymetry (Menezes et al. 2014).

In the South Indian Ocean (Figure 1), a westerly flowing current called the South Equatorial Current (SEC) exists. This current is largely supplied by the Indonesian Throughflow (ITF) (Godfrey 1996) via recirculations from the South Java Current (SJC) and the Eastern Gyral Current (EGC) (Sprintall et al. 2002). When the SEC reaches Madagascar (near 55 °E, 15°S), it splits into two branches, forming the Northeast and Southeast Madagascar Currents (NEMC and SEMC). A retroflection of the SEMC and a source farther to the west is shown to supply the South Indian Countercurrent (SICC) (Figure 1) (Schott, Xie & McCreary Jr 2009). Part of the eastward flow SICC also recirculates northwestward into the SEC (Domingues et al. 2007).

1.1.1 The Indonesian Throughflow water

The ITF brings warm fresh water from the Pacific Ocean into the Indian Ocean via the strongly mixed Indonesian Seas. The ITF flows between Australia and the southern boundary of the Asian continent and is one of the main links for water and heat exchange between the Pacific and Indian Oceans (Meyers, Bailey & Worby 1995). This flow is unique and influences both the currents and ocean biogeochemistry of this region (Talley & Sprintall 2005). As a result, the ITF is a vital contributor to the South Equatorial Current (SEC), the Leeuwin Current (LC) and the Eastern Gyral Current (EGC) (Menezes et al. 2013). Ayers et al. (2014), stated that the ITF contains a nutrient flux which is rich in nitrate. The nutrient flux enters into the Indian Ocean at the three main exit passages of the ITF (Lombok Strait, Ombai Strait, and Timor Passage), directly influencing the primary productivity in this region (Ayers et al. 2014).

1.1.2 The Eastern Gyral Current (EGC)

The Eastern Gyral Current (EGC) is a persistent eastward geostrophic flow (along 16°S-18°S) supplied by the recirculation from the ITF/SEC (Domingues et al. 2007) and retroflection from SEMC (Schott, Xie & McCreary Jr 2009). Menezes et al. (2013) concluded that the establishment and maintenance of the EGC is caused by salinity gradients between the freshwater input from the South Equatorial Current and saline subtropical waters. Total current transport has been calculated to be ~4.8Sv with transport intensifying throughout July – September (Domingues et al. 2007). A section of the EGC is joined by the SEC south of Java and carries relatively warm and fresh tropical water to the west coast of Australia where it connects with the Leeuwin Current (Meyers, Bailey & Worby 1995). Collectively this demonstrates that the EGC is an important contributor to the Eastern Indian Ocean (Waite et al. 2013)

1.2 Introduction to the Leeuwin Current

The eastern boundary of the South Indian Ocean lies along the West Australian coast (22°S–34°S) and is dominated by the Leeuwin Current system. The Leeuwin Current (LC) is composed of a poleward flow in the upper ocean (Cresswell & Golding 1980) and a deeper equatorward flow called the Leeuwin Undercurrent (Thompson 1984). Furthermore, (Furue et al. 2017) showed that the eastward flows of the SICC and EGC contribute a large proportion of the water mass that feeds into the Leeuwin Current system. In this section, we focus on the Leeuwin Current.

1.2.1 Characteristics and sources of the Leeuwin Current

The structure and characteristics of the Leeuwin Current have been explored in many studies (Cresswell & Golding 1980; Thompson 1984; Waite et al. 2007). It is a unique current because it is the only poleward flowing eastern boundary current in the world. The Leeuwin Current is considered to be driven by a large alongshore pressure gradient generated at the entrance of warm fresh tropical water carried by the ITF from the Pacific (Stuart Godfrey & Weaver 1991). A north-south pressure gradient extends across the Indian Ocean south of the SEC due to the geostrophic eastward flows of the South Indian Countercurrent (SICC) and EGC. Along other westerly coastlines, equatorward winds drive an offshore Ekman transport and upwelling against the coast which causes high productivity. However, this doesn’t appear to be true for the South Indian Ocean. In this scenario, wind-driven offshore Ekman transport is suppressed by the opposing eastward flow of the South Indian

Countercurrent (SICC) and EGC (Furue et al. 2017). This appears to limit significant upwelling along most of the west coast of Australia (Godfrey & Ridgway 1985).

The sources of the Leeuwin Current and associated pathways are constructed. Among the surface circulation of the Indian Ocean shown in Figure 1, there exists two eastward currents that are considered to be sources of the LC. These currents are the tropical Eastern Gyral Current (EGC) and the subtropical South Indian Countercurrent (SICC) (Domingues et al. 2007).

The SEC becomes more saline as it flows westward toward the point where it retroflects to join the EGC (Wijffels et al. 2002). As the EGC approaches the Australian coast, moving southward, it becomes cooler and saltier due to strong air–sea fluxes in the region (Doney, Large & Bryan 1998). Thus, the EGC becomes denser and may sink into deeper layer of the LC (Domingues et al. 2007).

The dynamic structure of the Leeuwin Current has been explored for two decades. Extensive research has been conducted on its momentum balance (Feng et al. 2005), eddy field (Waite et al. 2007), transport (Feng et al. 2003; Fieux, Molcard & Morrow 2005; Furue et al. 2017) and its vertical dynamic structure. The Leeuwin Current also displays a highly energetic mesoscale eddy field (Feng et al. 2005; Waite et al. 2007). It is suggested that the LC eddies are highly important components of the heat and momentum transport in the southeast Indian Ocean (Fang & Morrow 2003). The transport of the current has been explored which shows the annual change of the current (Domingues et al. 2007; Stuart Godfrey & Weaver 1991; Thompson 1984). The strength of the Leeuwin Current varies seasonally displaying increased intensity during the austral autumn and winter due to the presence of a strong pressure gradient and a weaker southerly wind (Cresswell & Golding 1980; Fieux, Molcard & Morrow 2005). In addition the El Niño/Southern Oscillation (ENSO) can also influence the strength of the Leeuwin Current (Pearce & Phillips 1988). Stronger flows are observed during La Niña years and weaker during El Niño events (Feng et al. 2003; Pearce & Phillips 1988).

1.2.2 Influence of the Leeuwin Current on local ecosystem and fishery

Any variation in the physical characteristics of the Leeuwin Current impacts local ecosystem dynamics. There have been multiple regional observations of biomass and primary production in the LC region (Hanson, Pattiaratchi & Waite 2005; Lourey et al. 2013; Rousseaux et al. 2012; Thompson, Wild-Allen, et al. 2011). Productivity along this current is important to the growth of reefs along the western continental margin (Collins, Wyrwoll & France 1991). It also has a major influence on the abundance of many species (Caputi et al. 1996). Other Southern Hemisphere ocean eastern boundary currents that process high nutrient surface water support extensive and productive finfish fisheries (Polovina, Howell & Abecassis 2008; Waite et al. 2019). In contrast, the west coast of Australia supports a higher abundance of invertebrate species due to the warm, fresh and low nutrient Leeuwin Current water (Caputi et al. 1996). The western rock lobster fishery is Australia's most valuable fishery (Feng et al. 2011). The strength of the LC is positively correlated with recruitment and catch of the western rock lobster (Figure 2) (Caputi & Brown 1993; Caputi et al. 2003; Pearce & Phillips 1988) in part due to the high level of eddy activity (Zheng et al. 2018) and associated phytoplankton production (Waite et al. 2019).

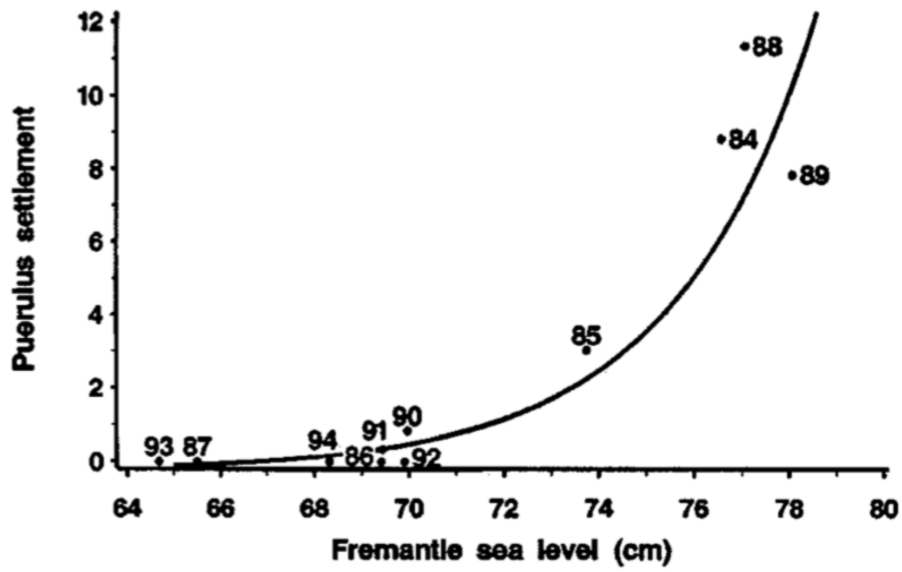

Figure 2. Relationship between annual Fremantle sea level (an index of the strength of the Leeuwin Current) and the annual rock lobster puerulus settlement at Cape Mentelle (mean number per collector), which commences later in the same year. The year is indicated by the number located along the curve (Caputi et al. 1996)

The Leeuwin Current significantly influences regional productivity and fisheries off the west coast of Australia (Feng, Waite & Thompson 2009). For example , it is known to impact pilchard spawning events and egg distribution which poses a significant management issue to these fisheries (Fletcher, Tregonning & Sant 1994). The LC also influences the recruitment of tropical reef fishes (Hutchins & Pearce 1994), scallop fisheries (Joll 1994) and stocks of anchovies (Lluch-Belda et al. 1989).

1.2.3 Nutrient in the Leeuwin Current

The LC differs from other eastern boundary currents at similar latitudes due to its poleward flow and low upwelling zones (Thompson 1984). Normally, eastern boundary currents flow toward the equator and are the most productive oceanic ecosystems in the world due to significant nutrient-rich upwelling (Thompson 1984). For example, the upwelling zones off the coast of Peru and Benguela drive strong primary productivity that supports large fisheries. In contrast, the Leeuwin Current (LC) shows weak upwelling due to the inclusion of warm fresh water from the north which deepens the thermocline and suppresses any upwelling(Smith et al. 1991). Additionally, onshore SICC and EGC flow against the wind-driven offshore Ekman transport further suppresses upwelling that decreases productivity (Thompson, Bonham, et al. 2011).

However, some particular nutrients are suggested to be carried with the Leeuwin Current. In particular, this current contains higher silicate content than the surrounding water masses. It is also moderately enriched in phosphate but limited in dissolved inorganic nitrogen (Lourey, Dunn & Waring 2006). The low nitrogen content of the LC potentially restricts biological productivity along the west Australian coastline (Feng, Waite & Thompson 2009). (Condie & Dunn 2006) showed that the phytoplankton biomass along the west coast of Australia is significantly less than other eastern boundary currents at similar latitudes (Thompson, Bonham, et al. 2011).

1.3 Sources of nutrients for regional productivity

Along the west coast of Australia, the biomass of flora and fauna is limited mainly by the availability of nitrogen (Lourey, Dunn & Waring 2006). Regionally, the productivity along west coast of Australia is shown to be less than other eastern boundary current areas (Condie & Dunn 2006), yet an annual shelf scale bloom of phytoplankton during Austral winter has been discovered (Figure 3) from many measurements (Feng et al. 2007; Feng, Waite & Thompson 2009; Lourey, Dunn & Waring 2006; Moore Ii et al. 2007). Figure 3 shows the winter bloom observed from satellite chlorophyll observations. The phytoplankton enhancements occur at different times with different sizes from north to south along the coast, which indicates that multiple factors can influence the winter bloom, including physical factors and biological factors (Feng, Waite & Thompson 2009).

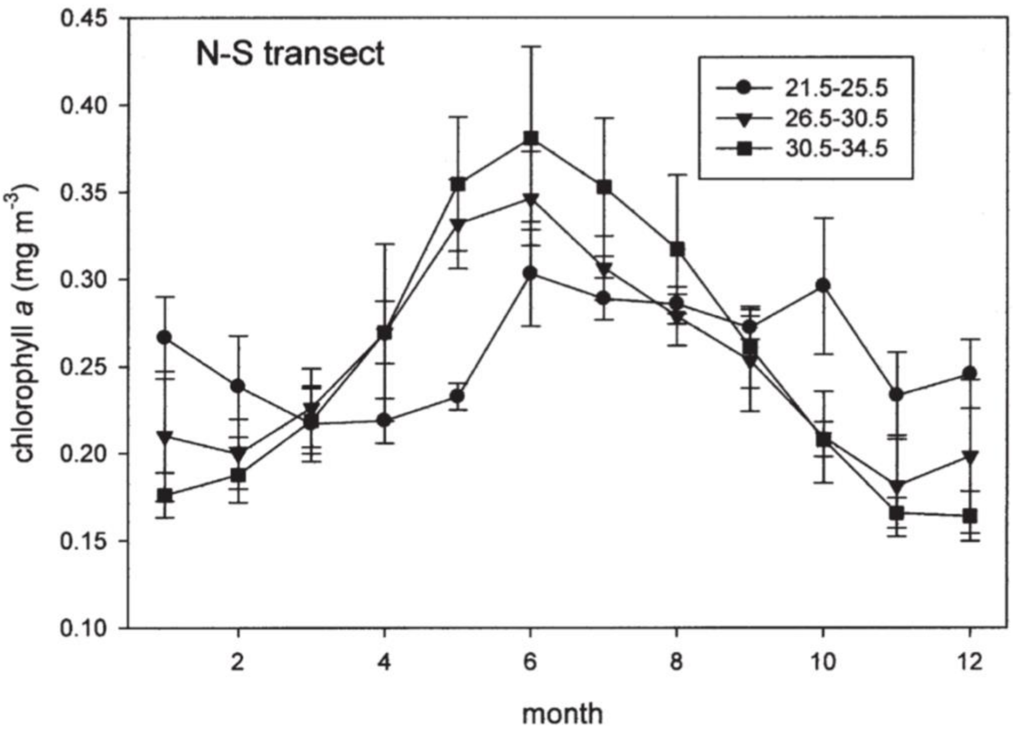

Figure 3. Monthly climatology of sea surface chlorophyll a concentrations. Data is averaged over three latitude bands on the continental shelf (approximately in the 100 and 1000 m depth range) off Western Australia. Derived from the 1997–2007 SeaWiFS ocean color satellite data.(Feng, Waite & Thompson 2009)

There are several speculative mechanisms for the incorporation of nutrients to supply the winter bloom (Feng, Waite & Thompson 2009). Firstly, localized enrichment from the continental shelf may contribute (Dietze, Matear & Moore 2009), where anticyclonic eddies transport nutrient dense waters (Paterson et al. 2008). Secondly, mesoscale eddies (in particular warm-core eddies) can enhance vertical mixing and horizontal transport of properties (Feng et al. 2007; Waite et al. 2007). Thirdly, other mechanisms could draw nutrients from below the thermocline up into the surface layer (Feng, Waite & Thompson 2009). It is thought that sporadic upwelling events are also considered to enhance the winter bloom (Hanson, Pattiaratchi & Waite 2005; Rousseaux et al. 2012; Wilson, Carleton & Meekan 2003). Also, nitrification below the mixed layer in anticyclonic eddies is conjectured to increase localized production (Paterson et al. 2008). Finally, a thin layer of water containing low dissolved oxygen and high nitrate (HNLDO layer) is a proposed nutrient source for midwinter bloom events (Thompson, Wild-Allen, et al. 2011). The magnitude of the midwinter bloom is proportional to the current strength, and the nutrients found in the HNLDO layer is sufficient to support the bloom (Feng et al. 2003).

1.4 The HNLDO layer and its effects

Although the LC generally contains low concentrations of dissolved inorganic nitrogen that correlates with the low biological productivity, it contains a thin layer of low dissolved oxygen (DO) and high nitrate concentration at ~100 m depth (Thompson, Wild-Allen, et al. 2011; Woo & Pattiaratchi 2008)). The source of this HNLDO layer was presumed to be offshore. The layer is thought to be isolated from the surface for a period that allows biological consumption of oxygen (via respiration) and nitrogen to produce a significant anomaly in DO and nitrate (Thompson, Wild-Allen, et al. 2011). The LC transports this layer southward at depth and it eventually mixes into the euphotic zone where photosynthetic active radiation (PAR) allows the available nitrate to support primary production. (Thompson, Wild-Allen, et al. 2011) proposed that mixing into the euphotic zone occurs by at least two mechanisms, the formation of warm core eddies or the surface cooling and deepening of the LC surface mixed layer into the HNLDO layer. Both these mechanisms are hypothesized to support the shelf-scale bloom during austral winter. If correct, this is an important mechanism vital to both the ecology and economy of Western Australia.

An alternative hypothesis (Rossi et al. 2013) is that the HNLDO layer forms rapidly and *in-situ* as the LC moves southward. (Rossi et al. 2013) noted the HNLDO was observed widely but did not show distinctive temperature and salinity (T/S) characteristics that would indicate the layer was carried in from a remote source. The authors suggested that the formation of the HNLDO layer may be caused by the accumulation of the remineralized surface organic matter. Furthermore, (Waite et al. 2013) suggested that the formation and maintenance of the HNLDO layer below the

LC is sourced from local biogeochemical processes (including surface nitrogen fixation, sinking/subduction, decomposition and nitrification). An observation of the low salinity Eastern Gyral Current (EGC) water beneath the surface LC may also play a key role in the formation of the HNLDO layer (Domingues et al. 2007). The aim of this research is to investigate whether the EGC is supplying the HNLDO layers to the Leeuwin Current.

1.5 Overview of the project

High resolution data from three transects through the EGC were collected to explore the current which allows a description of the watermass and velocity structure of the EGC and an estimation of the EGC transport of nitrate as well as heat, salinity, oxygen, volume transport.

The Leeuwin Current is an important current for western Australia as it plays a key role in the local ecosystem and fisheries. Many studies have been done to study the physical characteristics of the Leeuwin Current and the ecosystems in it. However, how the physical processes influence the biology and ecosystem in the area is less understood. The observed HNLDO layer is not well defined yet with an uncharted source. This study explores the EGC properties to see if it is a possible offshore source of nutrients that support the annual phytoplankton bloom within the Leeuwin Current. For the first time, the detailed properties across the EGC have been observed and the transport of the EGC can be estimated. The HNLDO layer in the EGC will be investigated as well.

1.6 Aims of the project

The aims of the project are:

(1) Describe the horizontal and vertical structure of the velocity field and watermass properties from observations across the EGC,

(2) Calculate the transport by the EGC of volume, heat, salt and nutrients,

(3) Determine whether the EGC can supply the high nitrate low dissolved oxygen (HNLDO) layer to the Leeuwin Current.

2 Data

2.1 The voyage data

2.1.1 Details of the voyage

In this study, data was collected onboard the *RV Investigator* (Voyage IN2019_V03) between May 13 and June 14, 2019. This voyage explored the physical, biogeochemical and ecological processes in the Southeast Indian Ocean. Its objectives including quantifying physical, chemical and biological properties along the 110°E line and investigating the sources of nitrogen to the region. The 110° E line of IN2019_V03 cuts across the EGC and SICC taking comprehensive observations of the currents from south to north. At the northern end of the 110° E line, the voyage explored three Triaxus tracks across the Eastern Gyral Current (EGC) to examine its velocity and watermass properties.

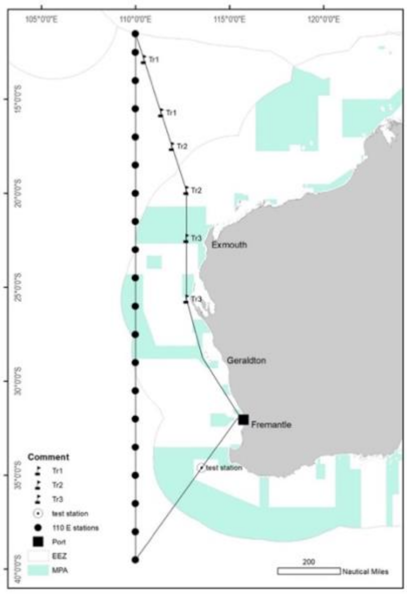

Figure 4. Voyage track for IN2019_V03 indicating test station, 20 CTD stations and 3 Triaxus tow sections. (RV Investigator Voyage Plan for IN2019_V03, 2019)

A Conductivity-Temperature-Depth (CTD) profiler was deployed wat each station along 110°E line. Stations were 1.5 degrees apart in longitude and profiled from the surface to the seafloor. A lowered Acoustic Doppler Current Profiler (LADCP) was also attached to the CTD rosette to measure current speed and direction at each depth. The positions of all stations along the transect were as similar as possible to those of a previous voyage conducted in the 1960s. Replicating sampling locations from the earlier voyage was to allow investigation of changes in oceanic properties over time. Figure 4 shows CTD stations and the planned position of the Triaxus tracks to cross the EGC in several places based on previous studies (e.g. Domingues et al. 2007, Menezes et al. 2013). During the voyage, the actual deployment positions of Triaxus were determined based on near-real-time satellite sea surface height (SSH) and surface current information. Based on this information we planned 3 crossings of the EGC such that the Triaxus crossed perpendicular to the EGC. Figure 5 shows the SSH and surface currents on the day of the first Triaxus tow with the planned paths for each track on that day (Phillips, personal communication)

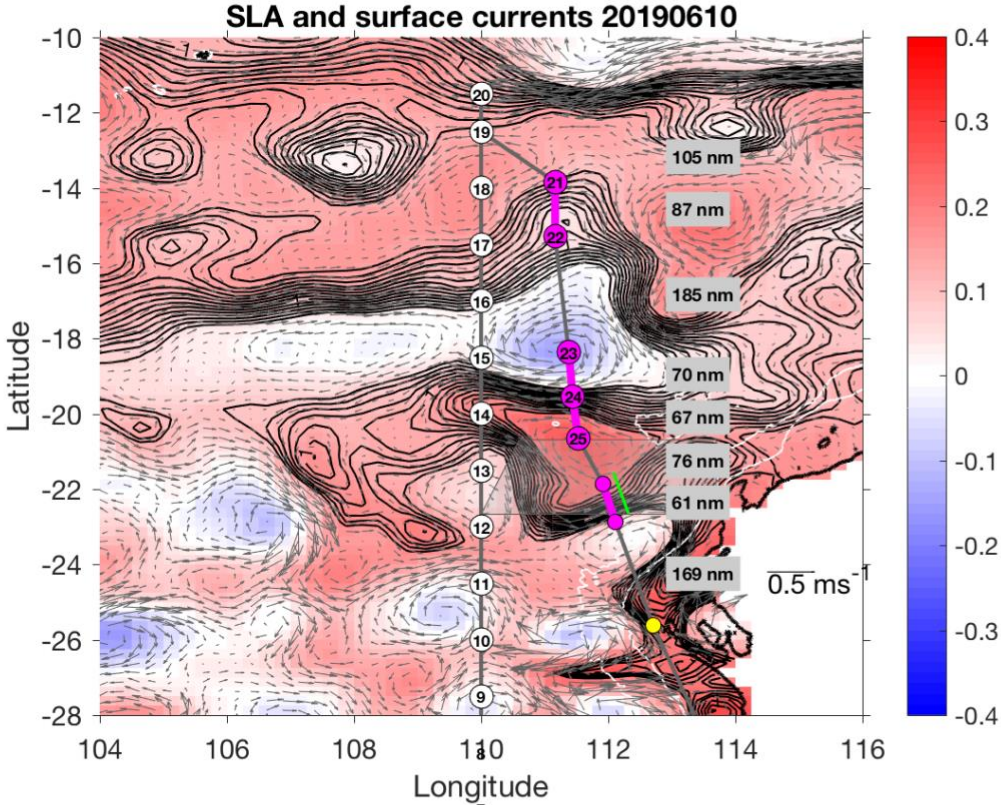

Figure 5. Figure from the voyage planning that gives the map of SSH and currents at the time of the Triaxus tows (Phillips, personal communication).). Black contours show sea surface height in the EGC with grey quivers showing the sea surface geostrophic current from satellite data. The magenta lines show the position of three Triaxus tracks, the circles with numbers indicate the CTD stations.

There were CTD stations at the start and end of Triaxus track 1 and at the start, middle and end of track 2. Track 3 was close to a marine park and no CTDs were taken there. CTD, Triaxus and ADCP data will be used in this study to explore the EGC and the associated physical properties.

2.1.2 Triaxus undulating towed platform

2.1.2.1 Triaxus sampling

Triaxus data was collected along three transects through the EGC. Triaxus is an instrument that is towed behind a vessel to provide high resolution data of water properties. In this study it profiled from the surface to a depth of 300m. The data obtained was analyzed in two ways. The track-format data records Triaxus data along the tracks as it profiles up (up cast) and down (down cast) through the water. This format records all of the measured parameters as a function of time only. The vertical cast data is transformed from the track data to separate each vertical profile from the surface to 300 m depth. The vertical cast data is derived by interpolating between consecutive up-cast and down-cast data to give vertical casts with parameters recorded as a function of time along the track (or position) and pressure, which is sketched in Figure 6.

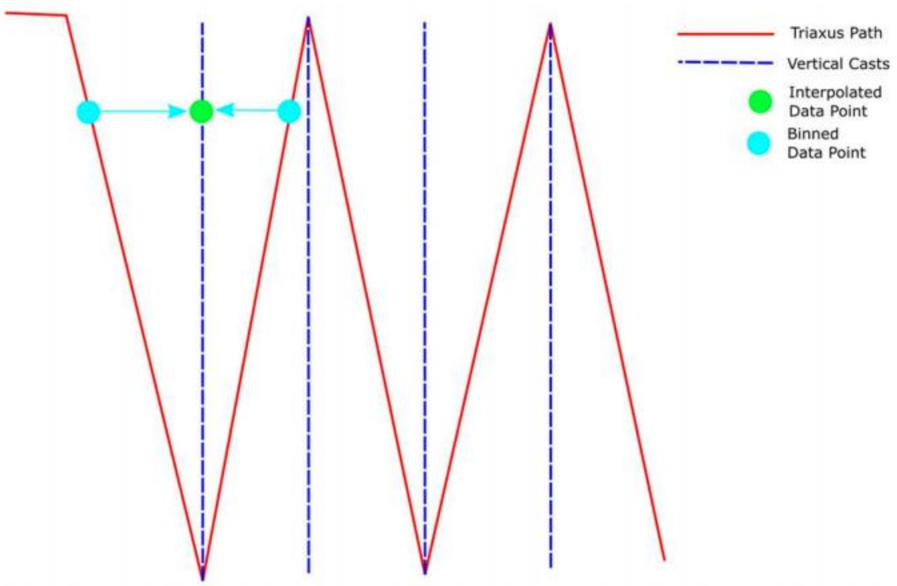

Figure 6. Demonstration for Triaxus path and conversion from track data to vertical casts data. (From in2019_v03_Triaxus_ProcessingReport)

The configuration of sensors attached to Triaxus during voyage IN2019_V03 is summarized in Table A4 (Appendix A). Two SBE43CTD units with dissolved oxygen sensors and a Cosine Photosynthetically Active Radiation (PAR) sensor, were installed on the Triaxus. An Eco-Triplet instrument that makes simultaneous measurements of chlorophyll, fluorescence and particle backscatter was also attached. A Laser Optical Plankton Counter (LOPC) was attached to the auxiliary serial channels but this data is not used in this study.

Data was acquired using Seabird's SeaSave acquisition software with Seabird SBE911+CTD#23. Temperature(℃), conductivity (converted to practical salinity units), pressure (dbar), oxygen (μM), PAR and nitrate data were collected. Details of the Triaxus configuration is in the Table A4(Appendix A).

2.1.2.2 Triaxus data from the voyage

Three deployments of the Triaxus were used to survey the watermass and velocity structure of the EGC in three different locations (Figure 5).

Figure 5 shows the three transects where the Triaxus was towed across the EGC – the northern transect (leg 1), the eddy transects (leg 2) and the southern transect (leg 3). The second deployment (eddy transect) was divided into two parts to allow a CTD station to be completed in the EGC. Information about the three Triaxus legs is shown in Table 1.

Table 1. Information of the Three Triaxus transects

Triaxus Deployment	time	Duration (hours)	latitude	longitude	Length of the transect (km)	notes
Start of leg 1	06/Jun 16:43:41	7	-13.807	111.161	164	The northern transect

End of leg 1	06/Jun 23:46:14		-15.295	111.181		
Start of leg 2	08/Jun 09:05:24	27	-18.306	111.375	263	The eddy transects, it was divided into two parts
End of leg 2	09/Jun 11:07:08		-20.673	111.528		
Start of leg 3	10/Jun 12:59:01	11	-21.812	111.911	133	The southern transect
End of leg 3	10/Jun 23:24:21		-22.996	112.137		

CTD stations to 1000 dbar were deployed at the start and end of the northern transect (leg 1) and at the start, middle and end of the eddy transect (leg 2). No CTD profiles were made for the southern transect (leg 3) since this was very close to a marine park and we had not obtained authorization to work in the marine park.

Water samples were collected to measure nutrients and chlorophyll concentration. Net samples were also performed at each location to examine the biological community composition. The CTD was deployed to ~1000m depth. For Triaxus, the maximum depth was ~300m. Data from CTD profiles was used to check on the quality of the Triaxus data and calibrate the sensors. The Triaxus data processing report is available from the Marine National Facility web site for the voyage (https://www.cmar.csiro.au/data/trawler/survey_details.cfm?survey=IN2019_V03).

2.1.3 CTD data

A total of 25 CTD stations were conducted during the voyage. Twenty stations were sampled along the 110°E line with the CTD being deployed twice at each station. The first CTD profile was early in the morning and extended from the surface to the sea floor (up to 5500 m in some locations). The second profile was shallower and deployed in the afternoon to a depth of 500 m. The focus for the afternoon profile was the biological sampling to look at the ecological community structure.

In addition, 5 CTD stations were distributed on the Triaxus legs (deployed to 1000 dBar). Two stations at each end of the northern Triaxus transect (leg 1) and 3 stations for the eddy transect (leg 2) (Figure 5)– one station at the start in the center of a cold-core eddy, one station at the end in the center of a warm core eddy, and one station in the middle where the EGC was flowing in a strong, narrow jet between the eddies.

CTD were fitted with 36 twelve-liter bottles on the rosette and data accessed using the SeaBird SBE911 CTD #23 and #24 sampler. The dual conductivity and temperature sensors were fitted on the CTD. The CTD rosette frame was additionally fitted with SBE43 dissolved oxygen sensors, Chelsea Fluorometer, PAR Sensor, Altimeter, Wet labs Transmissometer, upward and downward facing Teledyne Lowered Acoustic Doppler Current Profilers (LADCP) and user supplied Underwater Vision Profiler (UVP). Details of the CTD configuration are in the Table A5 (Appendix A). Information of the sensors that used to measure important properties in the project is shown in Table 2.

Table 2. Name and accuracy of sensors that measured important properties in the project.

Property	Model	Accuracy
Temperature	SBE3	±0.001°C
Conductivity	SBE4	±0.0003 S/m
Oxygen		

	SBE43	$\pm 2\%\ of\ saturation$
Nitrate	Satlantic SUNA V2	$2\mu M$
Current velocity	ADCP	± 0.5cm/s

2.1.4 The Acoustic Doppler Current Profiler (ADCP) data

A shipboard Acoustic Doppler Current Profiler (ADCP) was used to collect velocity information along the ship's track. The ADCP was installed at 2m depth below the waterline. Data was collected using University of Hawai'i Data Acquisition Software (UHDAS) and processed on the ship. Both the RDI Ocean Surveyor 150kHz ADCP and the RDI Ocean Surveyor 75kHz ADCP were run in narrowband mode. The higher frequency 150 kHz instruments measured eastward and northward velocity components down to approximately 300 m. The drop keel was at 2m below the waterline for the duration of the voyage. The 75 kHz ADCP provided velocity measurements to approximately 700 m but with a coarser sampling. The shipboard ADCP data was further processed at the end of the voyage by the Marine National Facility and the processing report is available from (https://www.marlin.csiro.au/geonetwork/srv/eng/search#!3bbb16fc-ecbe-4ad7-9f5d-74e5e052714c). In this study, we use the 150kHz ADCP data because of its higher vertical resolution over the depth range of Triaxus.

2.2 Supporting data

2.2.1 CSIRO Atlas of Regional Seas (CARS) data

CARS-2009 is a climatological dataset of long-term mean and seasonal cycles of ocean water properties across the globe. Containing gridded fields (0.5 degree latitude x 0.5 degree longitude) of temperature (°C), salinity (PSU), oxygen (ml/L), nitrate(umol/L), silicate (umol/L), and phosphate (umol/L). The climatology is constructed from all available CTD profiles and covers the period from 1950 through to 2009. CARS is derived from a high quality archive of all available historical subsurface ocean property measurements – primarily research vessel instrument profiles and autonomous profiling buoys (including Argo profiles of temperature and salinity).

In addition to CARS2009, which covers the full global oceans on a ½ degree grid, a 1/8-degree version was also constructed for temperature and salinity in the Australian region (90-180°E, 50°S to Equator). The monthly mean value of geostrophic velocity is also available, derived from the temperature and salinity fields.

2.2.2 Satellite data

The sea surface height data is accessed from the Australian Ocean Data Network (AODN). In this study, we use the sea surface height data that has been delayed mode processed. It contains gridded (adjusted) sea level anomaly (GSLA), gridded sea level (GSL) and surface geostrophic velocity (eastward and northward velocity components) for the Australasian region. GSLA is mapped using optimal interpolation of detided, demeaned, inverse-barometer-adjusted altimeter and tide gauge estimates of sea level. These methods are described on the AODN website (http://oceancurrent.imos.org.au/). The mean sea level which is estimated from the Ocean Forecasting Australia Model version 3 (OFAM3) over 18 years of model time was added to the GSLA for each day to get the total sea level for that day. The geostrophic velocities are derived from the total sea level each and are provided with the sea level data.

3 Materials and Methods

3.1 Absolute salinity, conservative temperature and potential density

Practical salinity and potential temperature were transformed into absolute salinity (g/kg) and conservative temperature (° C) as these units more accurately represent the thermodynamic characteristics of ocean. Absolute salinity is preferred as the thermodynamic properties of seawater are directly influenced by the mass of dissolved constituents, whereas practical salinity is dependent on conductivity only (McDougall and Barker, 2011). In this study, salinity and temperature were transformed into their absolute and conservative forms, respectively, using the Gibbs Seawater Library (GSW) MATLAB toolbox (http://www.teos-10.org/pubs/gsw/html/gsw_contents.html#3).

Furthermore, potential density was calculated using the GSW Toolbox. Seawater density is an important property that influences the position and equilibrium of a water parcel (Talley et al. 2011). Potential density is the density of a fluid particle at a reference pressure that moves adiabatically below the standard atmosphere, it is the density that is not influenced by changes of temperature and salinity (McDougall et al. 2012).

3.2 Rotation of velocity along- and across-transect components

Each of the Triaxus transects were designed to cross the Eastern Gyral Current perpendicular to the direction of flow (Figure 7). Since we are interested in the volume and water properties of the EGC, the measurement of velocity perpendicular to the Triaxus transect is vital. Velocity data collected from the shipboard ADCP were converted into a new coordinate system (Figure 8).

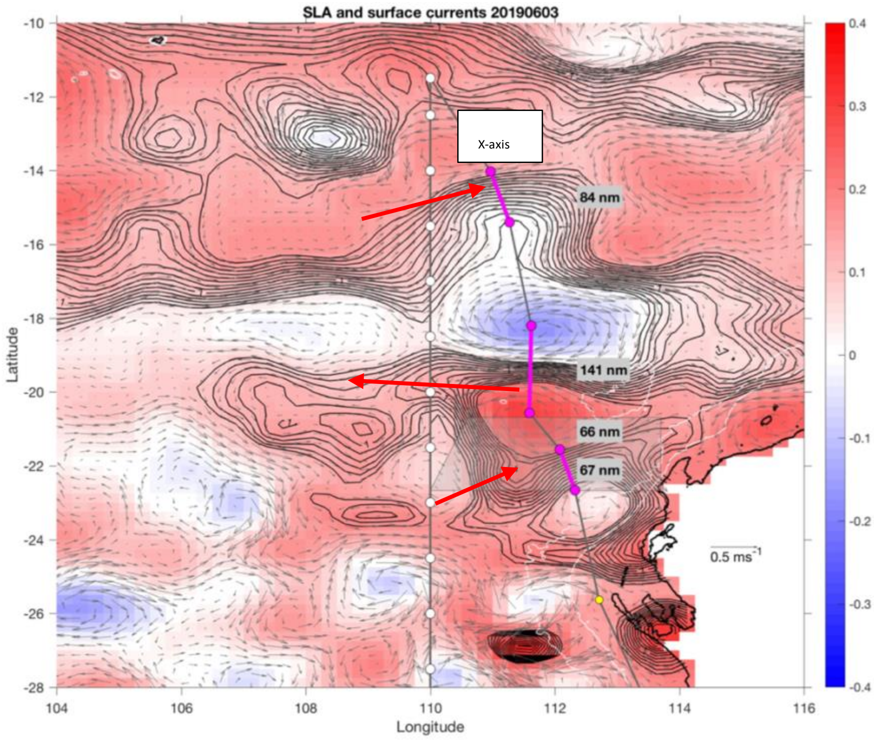

Figure 7. Intended Triaxus tows during the voyage on June 3rd (magenta lines). Red arrows show the direction of tracks for each of the transects. In the transformed coordinate, the red arrow shows the direction of the along-stream coordinate. The cross-stream direction is at an angle 90 degrees to the left of along-stream.

In the original coordinate system, the velocity is separated into two components, 1) eastward (original x-axis) and 2) northward (original y-axis) directions. It is necessary to transform the velocity data from the ADCP into a new coordinate system whose two axes are perpendicular to the Triaxus track (rotated x-axis) and along the Triaxus track (rotated y-axis) (Figure 8). Transformed velocity that is across the Triaxus tracks is used for the current transport calculation.

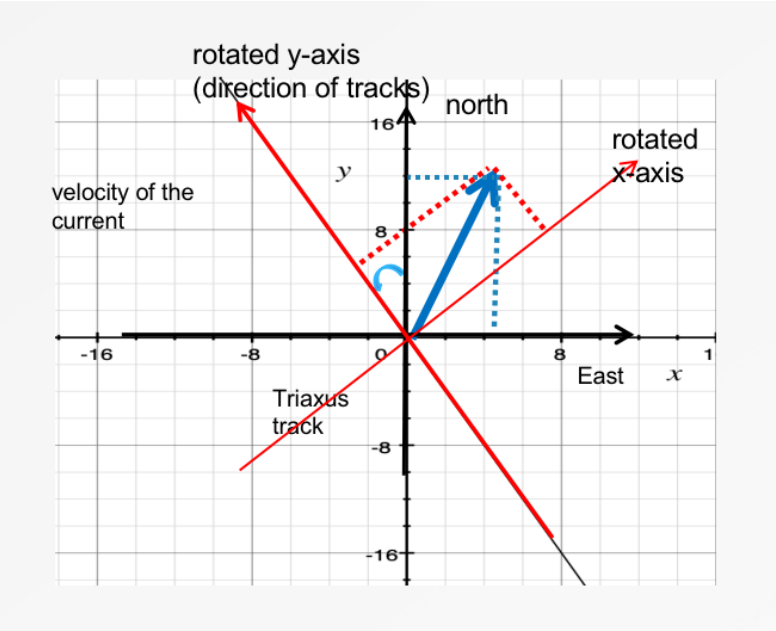

Figure 8. Schematic diagram of the rotation of the coordinate system. Black quivers represent the x and y axis of original coordinate. Red quivers represent rotated x and y axis. Blue quiver means the velocity of the current. It is separated into the north and east in the original coordinate (blue dash lines) and is separated into the rotated x and y axis that across and along the tracks (red dotted lines).

The velocity components are in a coordinate frame rotated with respect to eastward and northward directions. This is specified by the variable "rotation", which is the angle the transformed north coordinate makes with True North. The sign of rotation is dependent on the direction of the current. If rotation > 0 it means that the transformed north (rotated y-axis) is rotated eastward from True North (original y-axis). If rotation < 0 it means that the transformed north (rotated y-axis) is rotated westward from True North (original y-axis).

The rotation of coordinates is calculated by Equation (1).

$$ro = \pm \tan^{-1}\left(\frac{\Delta lon}{\Delta lat}\right) * 180/\pi \qquad (1)$$

Where, Δlon is the vertical distance between start and end point of the transect, Δlat is the horizontal distance between start and end point of the transect (Figure 9). For leg1 and leg 3, the rotated north axis is westward of true north, thus the sign should be negative. For leg 2 the rotated north axis is eastward of true north so the sign should be positive.

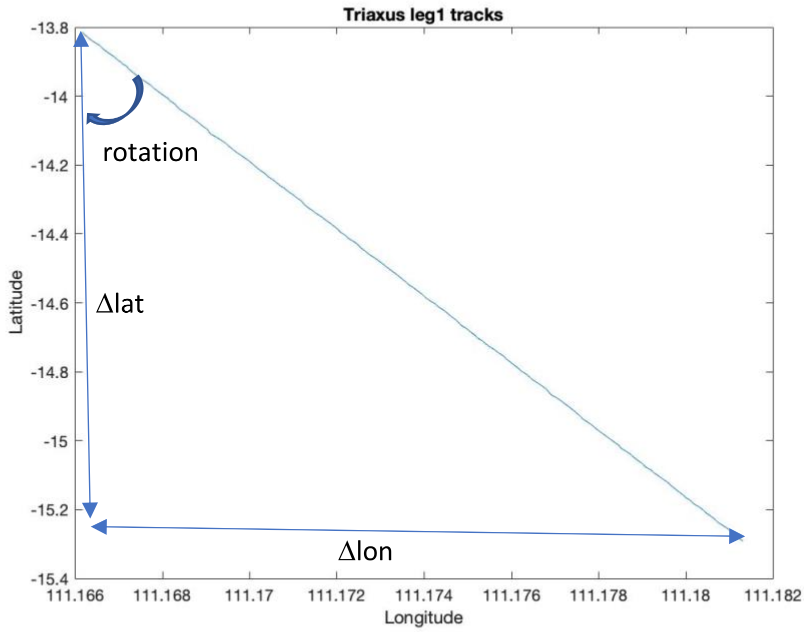

Figure 9. The Triaxus track 1 is considered as a straight line, the distance of latitude and longitude is calculated and is used to calculate the rotation.

The speed and direction can be calculated with the northerly (v) and easterly (u) component of velocity. Note that only the components are transformed, speed and direction are always relative to True North.

[speed, dir] = comp2speed(u, v, 0);

"comp2speed" is a MATLAB function from Helen E. Phillips (1996). It transforms velocity into speed and direction (Appendix C).

Then the rotated northerly velocity (v') and rotated easterly velocity (u') can be calculated with speed, direction and rotation.

[u’, v’] = speed2comp(speed, dir, rotation);

“speed2comp” is a MATLAB function from Helen E. Phillips (1996). It transforms speed, direction into rotated velocity corresponding to rotation (Appendix C).

3.3 Interpolation of Triaxus data onto a grid

The properties of the Triaxus cast data are available as profiles with depth distributed along the transect. The location of each profile can be treated as a position in latitude/longitude, or its distance from the start of the transect. In this study, we mainly use the distance in km to present the data profiles along the Triaxus tracks. The position and depth of each cast is not uniform along the transect. Therefore, it is necessary to convert the cast data into uniformly gridded data. We linearly interpolated the cast data onto a grid with vertical spacing in depth of $\Delta z=1$ m and horizontal spacing in distance along the transect of $\Delta x=500$ m.

3.4 Transport

The EGC is considered as the current with the across-track velocity > 0.02 ms^{-1}. Volume transport, temperature transport, salinity transport, oxygen transport as well as nitrate transport of EGC were calculated in each grid cell. The summed value in each grid cell is called the sum transport.

The volume transport in each grid-cell within the EGC is given by the product of the area of the cell times the cross-track velocity. Each cell is then summed over cells where the EGC is present (across-track velocity > 0.02ms^{-1}). This gives the total transport of the EGC in each of the three transects.

Volume transport Q (t) is given by Equation(2):

$$\boldsymbol{Q(t) = \sum \Delta x\, \Delta z\, v(x, z, t)} \qquad (2)$$

Where, Δx is the width of the grid cells (500m); Δz is the height of the grid cells (1m) and v is cross-track velocity. The unit of Q(t) is m^3/s which is equal to 1 x 10^{-6} Sverdrups (Sv).

To calculate heat transport, we use Equation (3):

$$\boldsymbol{Qheat(t) = \sum \rho\, Cp\, (T - Tref)\, \Delta x\, \Delta z\, v} \quad (3)$$

Where, ρ is the density of sea water (which we treat as a constant of 1025 kg m^{-3}). Cp is the specific heat capacity of seawater (the ratio of potential enthalpy to Conservative Temperature (J/ (kg K))). T is the conservative temperature and Tref is a reference temperature. In this study, the reference temperature is assumed to be 0 °C so that the heat transport is the total heat transport through the current. The unit of the heat transport is in Watts.

The salt transport, relative to a specified reference salinity Sref, is given by:

$$Qsalt(t) = \sum \rho(S - Sref)\Delta x \cdot \Delta z \cdot v \quad (4)$$

In equation (4), S is the absolute salinity (g kg^{-1}) and the reference salinity Sref is 0. Then the absolute salinity transport can be estimated using equation (4) in units of kg s^{-1}.

Oxygen and Nitrate transport are calculated using equation (5) and equation (6), respectively.

$$Qoxy(t) = \sum \rho \cdot O \cdot \Delta x \cdot \Delta z \cdot v \quad (5)$$

$$Qnit(t) = \sum \rho \cdot N \cdot \Delta x \cdot \Delta z \cdot v \quad (6)$$

Where, O and N are the concentration of oxygen and nitrate (µmol/L), respectively. The unit for the oxygen transport and nitrate transport is µmol/s.

3.5 The nitrate data

The nitrate data is measured with a sensor called Satlantic SUNA V2 attached to the Triaxus.

Until the submission of the thesis, the nitrate data from Triaxus was not available in the cast format and was uncalibrated. In this project, the relationship between nitrate and oxygen concentration is used to simulate the concentration of nitrate.

From Figure 10, the profile from CTD data shows that in the depth about 150m, the low dissolved oxygen concentration is related to the high nitrate concentration.

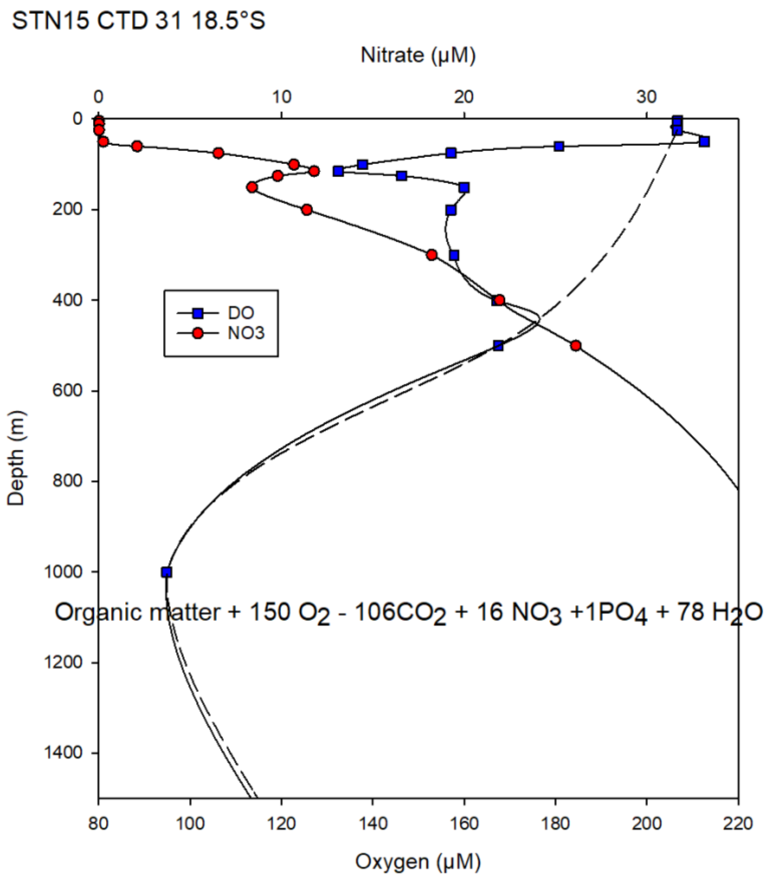

Figure 10. Profiles of nitrate concentration (µM) and oxygen (µM) from CTD station 15 along the 110E line with the latitude 18.5℃S. (From Peter Thompson individual)

The relationship between the nitrate and oxygen concentration has been further tested for the top 100m as well as top 300m using the data from the voyage which is shown in Figure 11 and Figure 12 below.

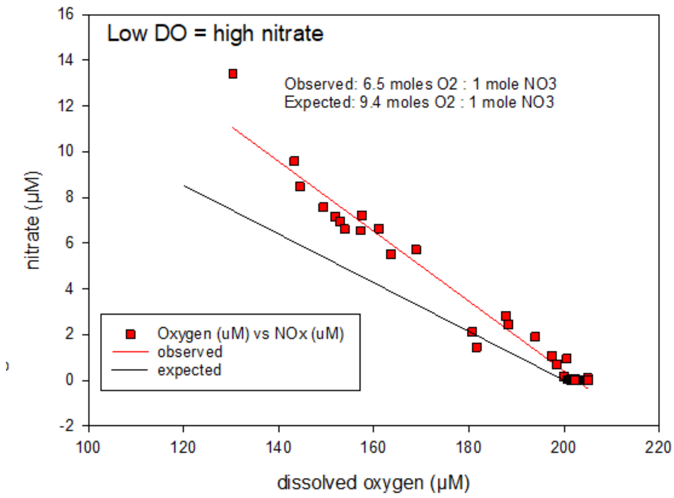

Figure 11. Observed and expected linear correlation between dissolved oxygen and nitrate concentration in the top 100m. (Thompson, Wild-Allen, et al. 2011)

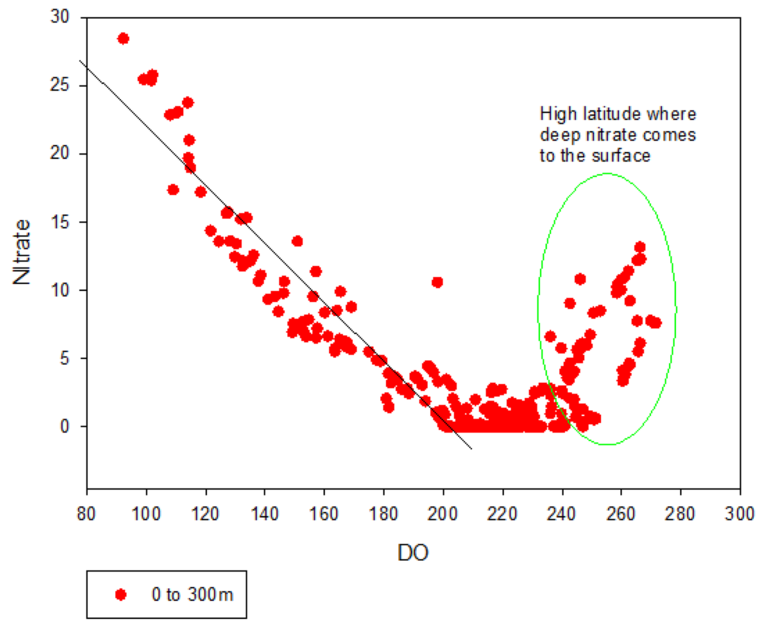

Figure 12. . Correlation between nitrate and dissolve oxygen in the top 300 m all stations along 110E from Voyage IN2019_V03. (From Peter Thompson individual)

As a result, it is reasonable to draw the conclusion that the nitrate-dissolved oxygen relationship is consistent in this region for top 300m. The rising NO3 from stations further south than 32°S is ignored (green ellipse, Figure 12). This is where high nitrate water comes right to the surface and is therefore saturated with DO.

According to Thompson, Wild-Allen, et al. (2011), the theoretical slope of DO:NO3 is 9.4:1 and observed slope of DO:NO3 is 6.5:1. This relationship provides the estimated nitrate with a decline in DO of 6.5 μmole expected for 1 μmole of nitrate. For the purpose of this study, the ratio 6.5:1 will be used to simulate nitrate concentration from the Triaxus dissolved oxygen measurements.

4 Results

Information on the property and velocity distribution of vertical sections along the 110°E line is displayed in Figure 13. Furthermore, vertical sections of velocity across three transects of EGC are used to identify the location of the main flow to investigate the horizontal and vertical structure of watermass properties in the EGC. Transport of volume, heat, salinity and oxygen are estimated. Finally, variation in the strength and position of EGC for one year (2019) is used to investigate current seasonality.

4.1 Vertical sections along 110 °E

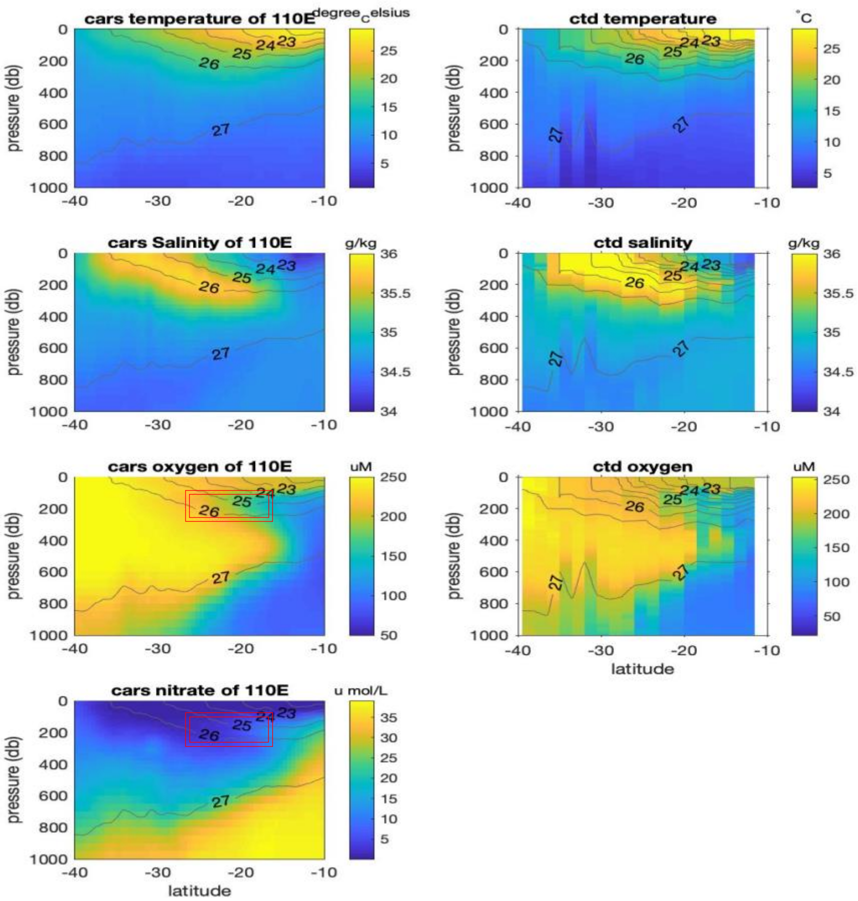

Figure 13. Temperature, salinity, oxygen and nitrate profiles from CARS along 110E line (left); Temperature, salinity, oxygen profiles from CTD along 110E line (right). Contours show the density of sea water. The area inside red border is the observed low oxygen layer and high nitrate layer.

By examining the profiles along the 110°E line using CARS annual average data, the average field of water properties along 110°E is shown (Figure 13, left panels). At lower latitudes about 10°S to 20°S, warm and fresh water are distributed on the top layers with lower density. The low salinity water is tropical surface water originating from the Indonesian Throughflow. At higher latitudes around 35°S-25°S, higher salinity and lower temperatures at the surface are observed. With a higher density, this water sinks below the less dense water as it moves northward, becoming the Subtropical Underwater (STUW). From the CARS oxygen section, we notice that a relatively high oxygen layer moves northward from 40°S beneath the STUW. This is the recently formed Subantarctic Mode Water (Woo & Pattiaratchi 2008). The layer thins as it moves northward and becomes cooler and less saline.

At 10°S -20°S, a low oxygen layer can be observed between 100-200 m depth. It illustrates that there exists a persistent low oxygen layer, as it is present in the long-term average of all observations in CARS. The CARS nitrate section shows that this low oxygen layer occurs in nearly the same position as the high nitrate layer. The nitrate section shows that very low concentration of nitrate appears in the upper compared to the deeper ocean. The shallow layer of high nitrate and low oxygen is surrounded by lower nitrate values above and below.

The sections of temperature, salinity and oxygen along 110°E line are also explored using the CTD station data from voyage IN2019_V03 (Figure 13, right). The section shows a snapshot of properties along this line in May and June of 2019 when the voyage went across the ocean from south to north. Compared to the profiles from CARS, the distribution of the temperature, salinity and oxygen has similar features at the time of the voyage. This elucidates that the large-scale features of the ocean water masses in this region are stable. However, when we look at the detail in the section from the voyage (Figure 13, right), we see smaller-scale variations. These are due to seasonal and interannual variations and eddied that are smoothed out in the CARS average fields. For example, between 30°S -35°S, two cyclonic (cold-core) eddies can be observed that lift up isopycnals, drawing up colder, fresher, low-oxygen waters from below in the CTD sections (Figure 13, right).

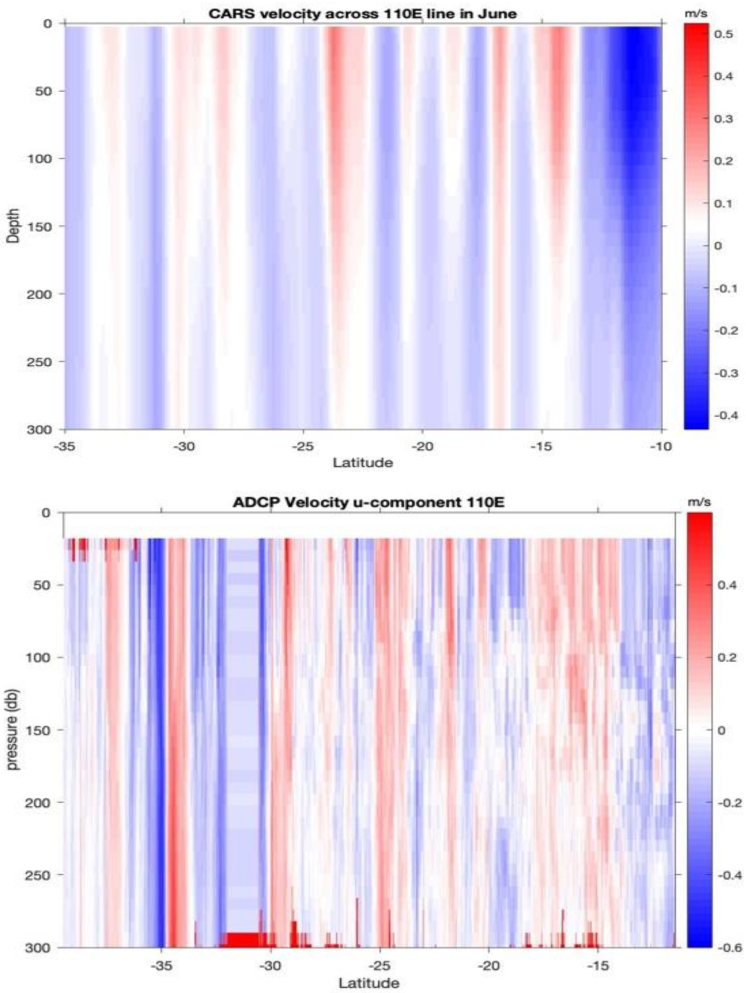

Figure 14. Mean eastward component velocity across 110E line in June from CARS (top); eastward component velocity across 110E line measured with the onboard ADCP during IN2019_V03 (bottom).

The mean geostrophic velocity for each month and the long-term annual mean velocity can be calculated from the CARS temperature and salinity data. Figure 14 shows the eastward component of velocity (June) from CARS (left panel) and the eastward component of velocity measured with onboard ADCP during the voyage in May-June 2019 (right panel). There are some clear differences in the strength and distribution of currents across the 110°E line between the long-term average (June) and the snapshot from the voyage. A strong westerly current between 10°S and 14°S is known as the South Equatorial Current (SEC). More to the south around 14°S to 17°S, the eastward flowing current shown in red color is the EGC, which transports water from SEC and ITW toward the west coast of Australia. The high nitrate and low oxygen layer shown in the CARS section (Figure 13) can be transported eastward towards Australia and possibly into the LC via the EGC. A longer period view can be shown that uses mean seasonal CARS velocity as well as daily satellite data. This will be discussed in Section 4.3.

From Figure 13, the existence of the low oxygen layer between 10ºS and 20ºS is verified in both measurements from CARS and from the voyage CTD data. The high nitrate layer associated with the low oxygen layer is also confirmed from CARS data. Moreover, a relationship between oxygen and nitrate in the HNLDO layer is shown (Figure 15).

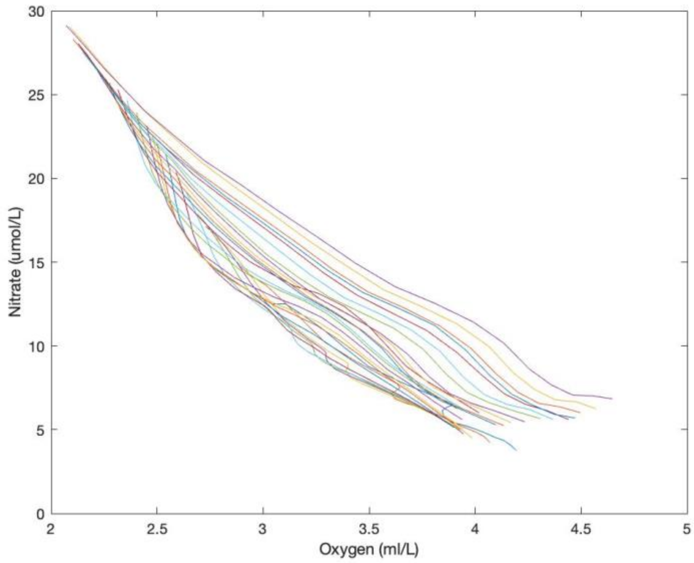

Figure 15. Nitrate and oxygen relationship from CARS in the HNLDO layer. Each line corresponds to a different point between 10S-20S and 100-300m.

The nitrate and oxygen relationship noted in Figure 13 identifies the HNLDO layer that we wish to examine. Using CARS data from 100-300m depth and 10ºS-20ºS latitude, there exists an approximately linear relationship between oxygen and nitrate (Figure 15). This relationship can be used to simulate the nitrate concentration based on the oxygen concentration in the HNLDO layer.

4.2 Surface observations at the time of the voyage

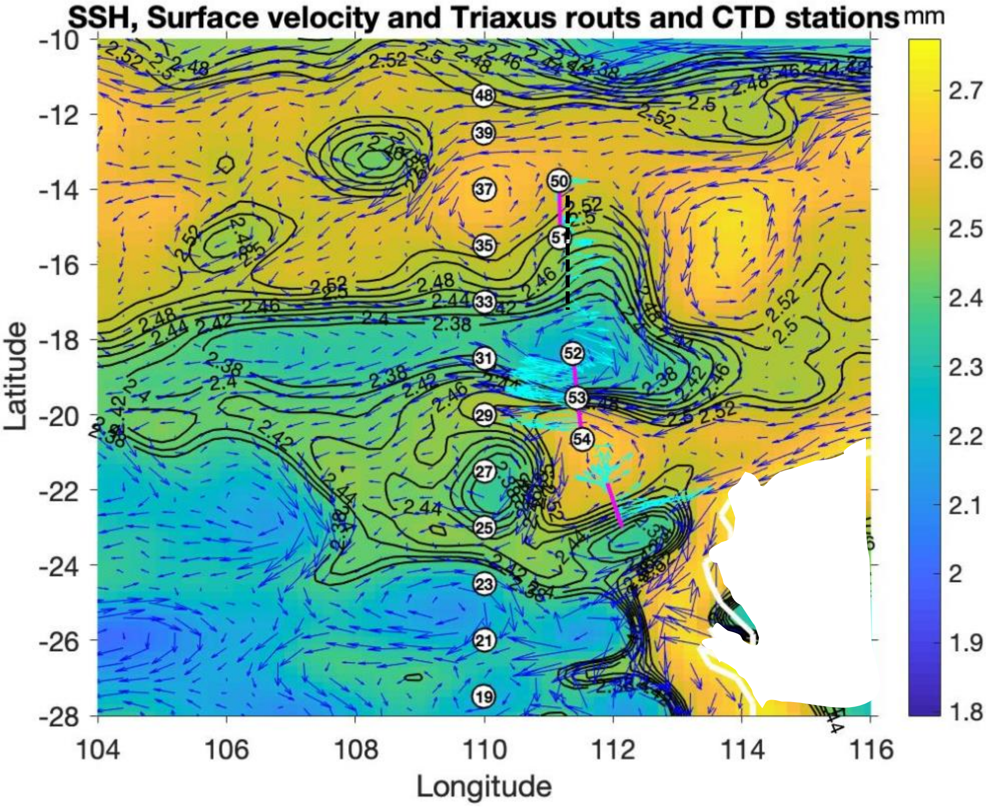

Figure 16. The sea surface height at 06-June-2019 when the first leg of Triaxus was conducted. The main the sea surface height features during the other Triaxus deployments is similar to the situation at 06 June. Black contours show sea surface height with blue quivers showing the sea surface geostrophic current from satellite data. The cyan quivers show the surface current from shipboard ADCP. The magenta lines show the position of three Triaxus tracks, the white circles show the CTD stations. Surface current vectors from satellite are plotted at every second grid point. Surface current from ADCP is real-time data with one vector plotted every 15 minutes along the track. The black dash line shows the position where the leg 1 should be to cross the entire current about 14°S-18°S.

From satellite sea surface height (SSH) data (Figure 16), the position of the EGC during the voyage can be observed. The SSH contours drawn in the figure (black lines) are those that highlight continuous flow from west of the 110ºE line and into the LC. The first leg of Triaxus does not fully cross the current, whereas leg 2 and leg

3 do. The ADCP current vectors (cyan color) indicate that the strongest section of the current is south of the leg 1 transect.

The reason for the missing part of the EGC in leg 1 is that the position of the three tracks was decided with real-time satellite observations and when eddies are nearby, the conditions can rapidly change. Moreover, the final delayed-mode SSH data (Figure 16) interpolates across observations before and after the day of interest and gives a more reliable position of features. Leg 2 was positioned to cross the very strong flow between a cold-core eddy to the north and a warm-core eddy to the south. Leg 3 crossed the EGC where the current intensity was not as strong as the current intensity in leg 2. In leg 3 the current was directed toward the coast potentially flowing into the Leeuwin Current.

4.3 Subsurface Structure of the Eastern Gyral Current

4.3.1 Velocity Structure

4.3.1.1 Triaxus Leg 1

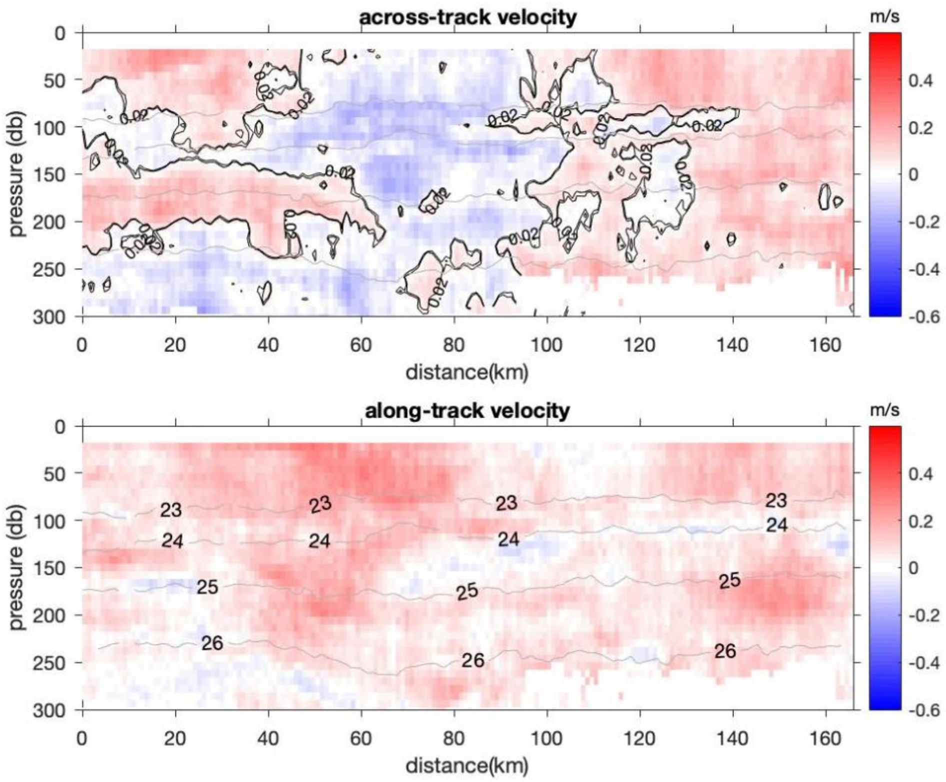

Figure 17. Current velocity from shipboard ADCP along Triaxus leg 1. The upper panel shows the across-track velocity (flow in the direction of the EGC), the lower panel shows the along-track velocity (flow perpendicular to the EGC). 0 km distance is the northern end of the line, and increasing distance indicates movement southward. In the upper figure, the black contour shows the 0.02m/s velocity, any velocity that higher than 0.02 m/s is assumed as the EGC. The grey contours are potential density contours(range from23-26) relative to the sea surface.

The ADCP velocity profiles match well with the surface current shown in Figure 16. Due to the track of leg 1 not completely crossing the northern section of the current, we used ADCP data that is further south than the Triaxus leg 1, where the EGC was exactly located (black dash line in Figure 16) at 14°S to 18°S. Figure 18 shows the velocity section from 14°S to 18°S recorded by the shipboard ADCP. The 400km distance in the x-axis covers the latitude range 14°S to 18°S. Hereinafter, the tracks of ADCP that cross the EGC from 14°S to 18°S is considered as the simulated leg 1. Only the ADCP velocity data can be obtained on this simulated leg 1 as it does not coincide with the Triaxus sampling.

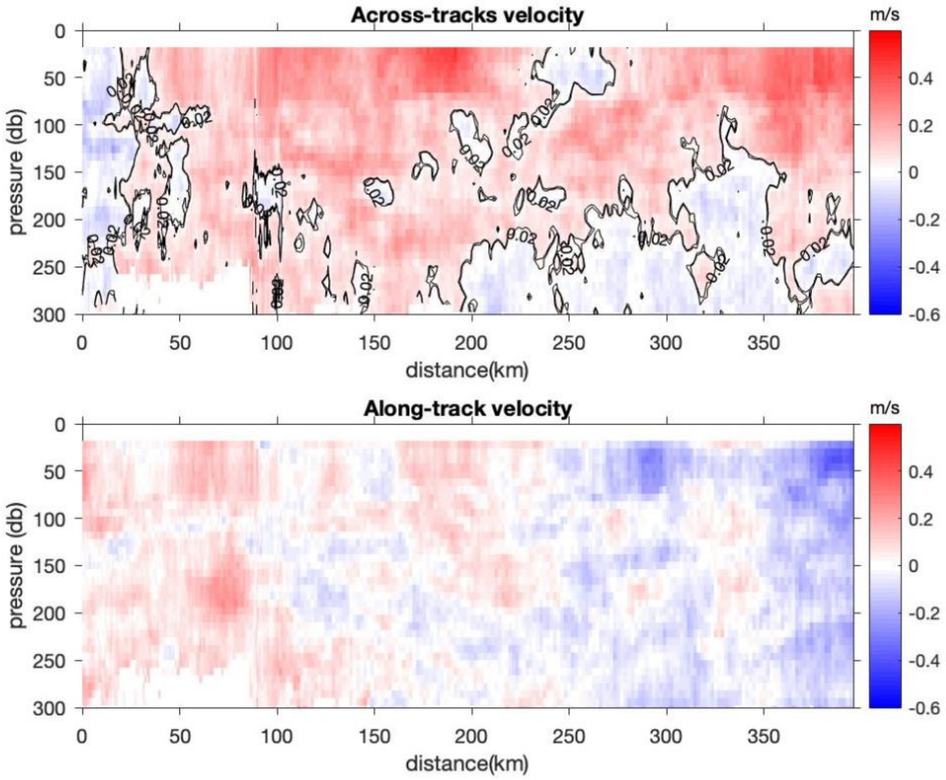

Figure 18. Velocity sections across the simulated leg 1 of the current from 14°S to 18°S. The upper figure shows the cross-track (EGC) velocity, the lower figure shows the along-track. 0 km distance is 14°S, and increasing distance indicates movement southward to 18°S. In the upper figure, the black contour shows the 0.02m/s velocity, any velocity that higher than 0.02 m/s is assumed as the EGC.

From the simulated leg 1(Figure 18), the velocity of the current shows a similar strength as leg 2 and leg 3 (Figure 19, 20). This can be then used to simulate the full volume transport of leg1. However, Triaxus didn't get across part of the simulated leg 1, therefore heat, salinity, oxygen and nitrate transport cannot be estimated.

4.3.1.2 Triaxus Leg 2

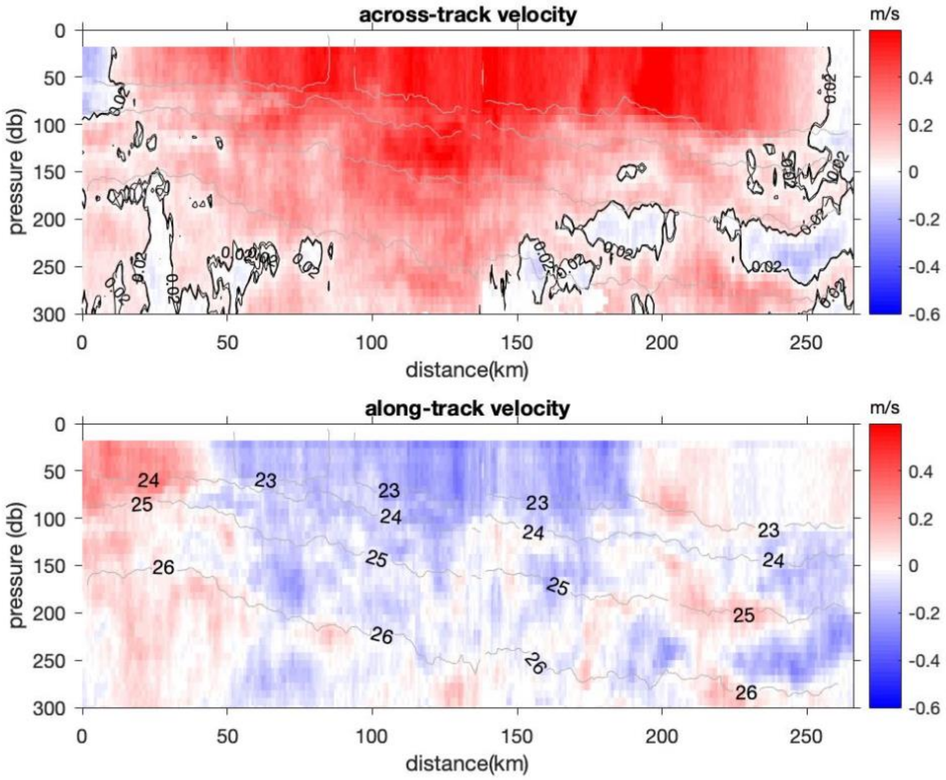

Figure 19. Current velocity from shipboard ADCP along Triaxus leg 2. The upper panel shows the across-track velocity (flow in the direction of the EGC), the lower panel shows the along-track velocity (flow perpendicular to the EGC). 0 km distance is the northern end of the line, and increasing distance indicates movement southward. In the upper figure, the black contour shows the 0.02m/s velocity, any velocity that higher than 0.02 m/s is assumed as the EGC. The grey contours are potential density contours(range from23-26) relative to the sea surface.

The velocity section from leg 2 shows the Triaxus tow completely crossed the EGC in leg 2 (Figure 19). This current shows a high strength up to 0.5m/s in the surface and the along-track velocity is weak at each end of the track.

4.3.1.3 Triaxus Leg 3

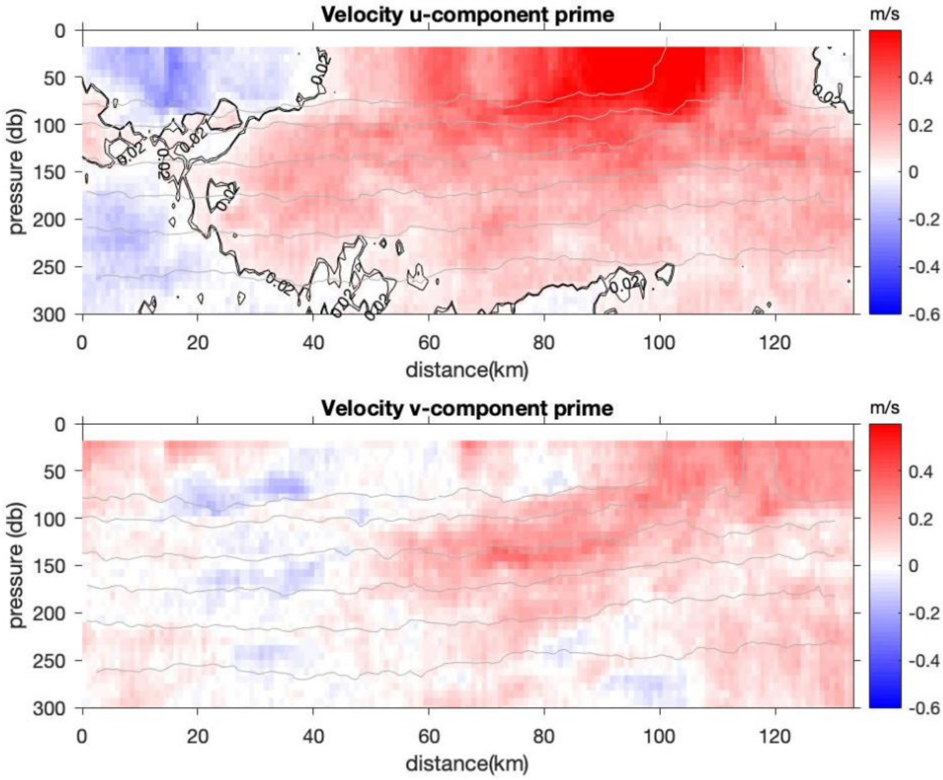

Figure 20. Current velocity from shipboard ADCP along Triaxus leg 3. The upper panel shows the across-track velocity (flow in the direction of the EGC), the lower panel shows the along-track velocity (flow perpendicular to the EGC). 0 km distance is the northern end of the line, and increasing distance indicates movement southward. In the upper figure, the black contour shows the 0.02m/s velocity, any velocity that higher than 0.02 m/s is assumed as the EGC. The grey contours are potential density contours(range from23-26) relative to the sea surface.

The leg 3 velocity section has a surface current velocity nearly 0.5m/s. The intensity of the current from leg 3 is similar to leg 2. The current becomes weaker with increasing depth and at the edges of the track.

We identify the EGC as the regions where across-track velocity is greater than 0.02 m s^{-1}. From all the current profiles along three tracks, we can observe a current with a relatively high surface velocity and strong across-track velocities extending to 300 m depth. relative high intensity that can deliver water volume, heat, salt, oxygen and nutrients to the LC. The contour of 0.02 m s^{-1} neatly separates the stronger along-stream flow of the EGC from regions of weaker current and regions where the current flow is not aligned with the EGC. We therefore use the criteria of along-stream flow >0.02 m s^{-1} as the footprint of the EGC for watermass analysis and calculation of EGC transport.

4.3.2 Watermass Properties

Triaxus was towed through the EGC in positions shown in Figure 16. The vertical sections of temperature, oxygen, salinity and potential density from all three tracks are shown Figures 21 (leg1), 22 (leg 2) and 23 (leg 3). The anomaly of the properties relative to the mean profile from each section are shown in the right panels of Figures 21, 22 and 23.

4.3.2.1 Triaxus Leg 1

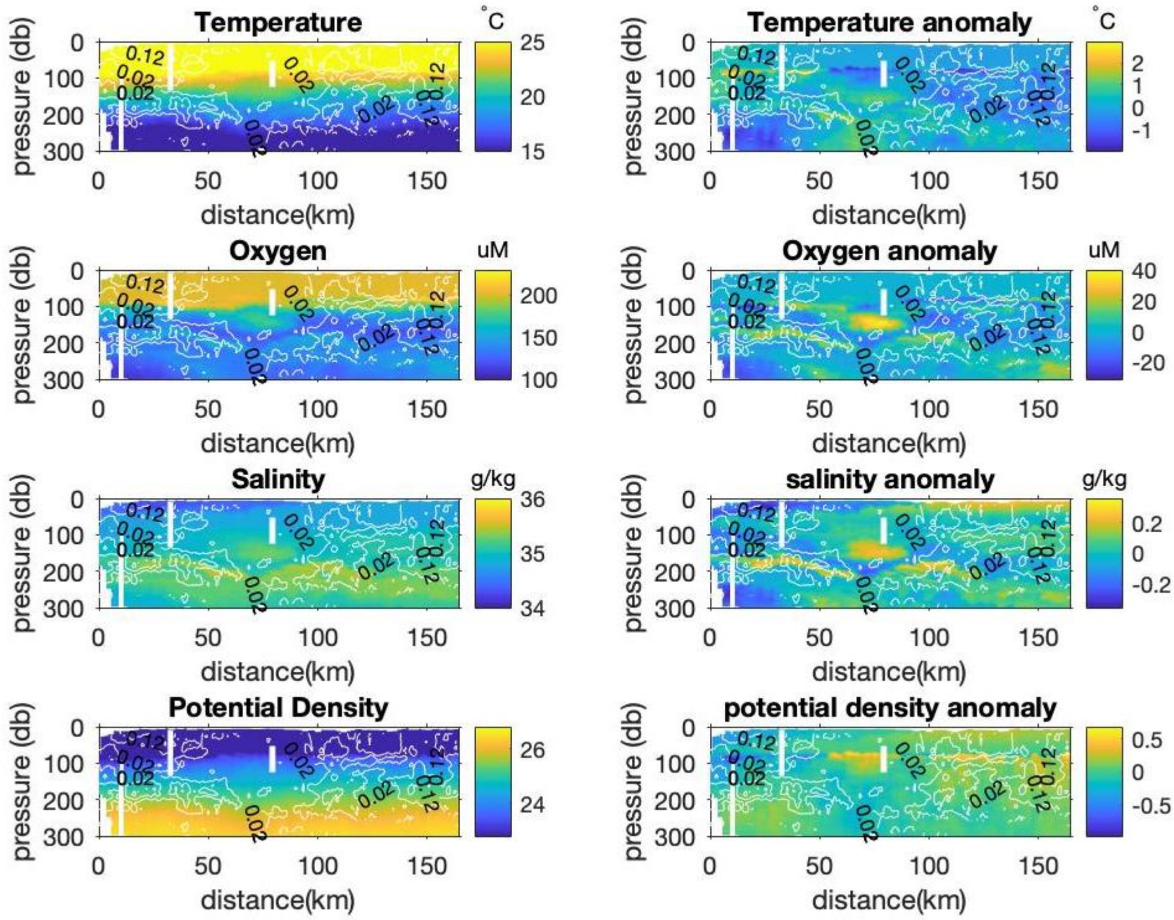

Figure 21. Vertical section of conservative temperature, dissolved oxygen, absolute salinity and potential density from Triaxus leg 1 (left) and their anomaly profiles (right). 0 km distance is the northern end of the line, and increasing distance indicates movement southward. White contours show across-track velocity from shipboard ADCP in units of m/s.

Along leg 1, warm, fresh and oxygenated (200µM) water is distributed on the surface (to 100m depth). Under this (100-200m), a very thin layer of lower oxygen (~100 µM) water can be observed. The potential density plot indicates strong stratification between 100 and 200 m, indicating that less vertical exchange is likely to occur in this area. The low oxygen layer is found in the part of the transect where the EGC is flowing eastward with speeds of 0.2 ms^{-1}. This suggests that the low oxygen layer is possibly delivered from another area instead of being formed at depth and upwelling, or being formed *in situ* by biological activity.

4.3.2.2 Triaxus Leg 2

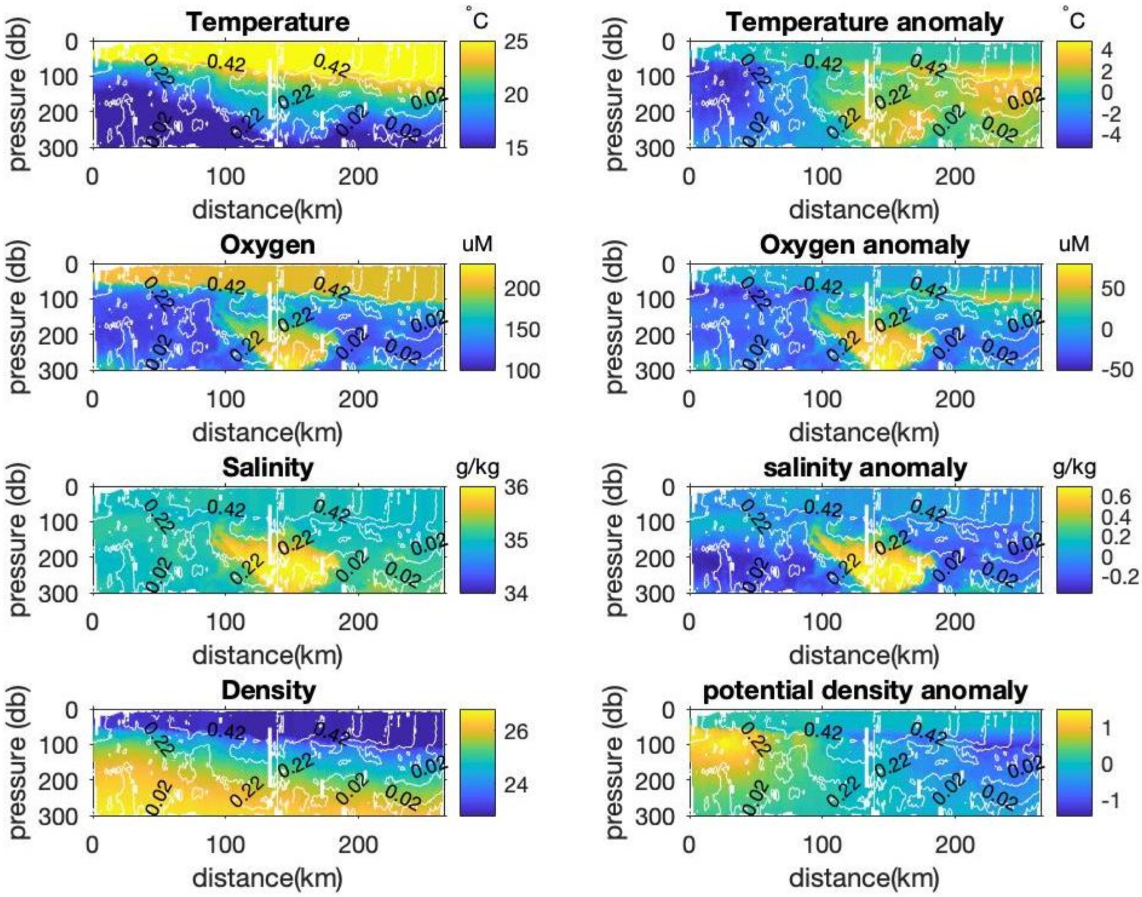

Figure 22. Vertical section of conservative temperature, dissolved oxygen, absolute salinity and potential density from Triaxus leg 2 (left) and their anomaly profiles (right). 0 km distance is the northern end of the line, and increasing distance indicates movement southward. White contours show across-track velocity from shipboard ADCP in units of m/s.

Along leg 2, surface temperature becomes cooler as the voyage moves southward. The potential density contours also slope southward which shows that it depends strongly on the temperature. It is noticeable that at the middle of leg 2, a water mass with high salinity and oxygen is present at 200-300m depth. According to the CARS data section (Figure 13) it is likely that this is the saline subtropical underwater formed in the subtropics and flowing northward below the surface (Woo & Pattiaratchi 2008). Between the high oxygen water mass at the surface and below 200 m, a low oxygen layer at 100-200m depth exists. Both the saline subtropical underwater and the thin low oxygen layer are carried by the EGC, which in this section has along-stream speeds of up to 0.5 ms^{-1} at the surface and >0.2 ms^{-1} at 100-200 m depth .

4.3.2.3 Triaxus Leg 3

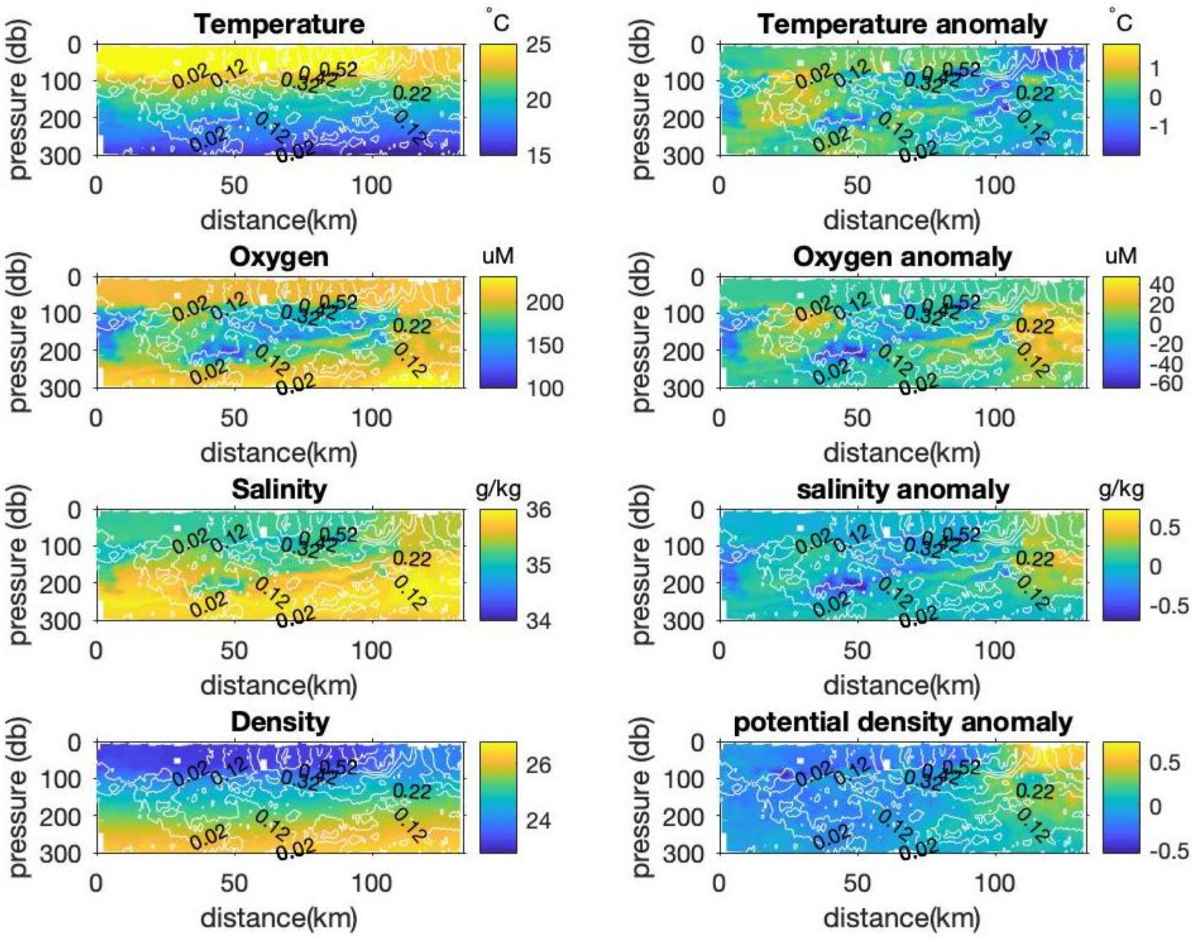

Figure 23. Vertical section of conservative temperature, dissolved oxygen, absolute salinity and potential density from Triaxus leg 3 (left) and their anomaly profiles (right). 0 km distance is the northern end of the line, and increasing distance indicates movement southward. White contours show across-track velocity from shipboard ADCP in units of m/s.

Along leg 3, surface water becomes cooler and saltier in the higher latitudes. In the southern part of the leg the surface water becomes dense causing the saline cool water to sink. From the oxygen section, the low oxygen layer is still present. The deeper high salinity, high oxygen layer is also present, however, it occurs across the full distance of the transect, not only within the EGC. This suggests that the subtropical underwater is more common in this region and does not rely on the EGC flow to arrive at this location. In leg 1, the subtropical underwater is not evident, or perhaps weakly present, and in leg 2 it was only present in the strong flow of the EGC and not in the rest of the section.

The low oxygen layer can be observed clearly between 100m and 200m depth in leg 2 as well as in legs 1 and 3 (Figures 21, 22 and 23). It confirms the existence of a low dissolved oxygen layer in the EGC. However, due to the strong negative correlation between oxygen and nitrate (Figure 11,12,15), we believe that there also exists a high nitrate layer in the same location.

4.3.3 Transport

The transport at every grid is dependent on the current velocity. The patterns of heat, salinity and oxygen transport are similar to the volume transport. Here, we only present the volume transport of the three legs. The transport of other properties can be found in Appendix B (Figure B28-B36). These patterns support the view that the EGC transports heat, salinity, oxygen as well as nutrients along its path. The total transport in the three transects is important to investigate as it tells us how much of each property is transported by the EGC and could be entering into the LC .

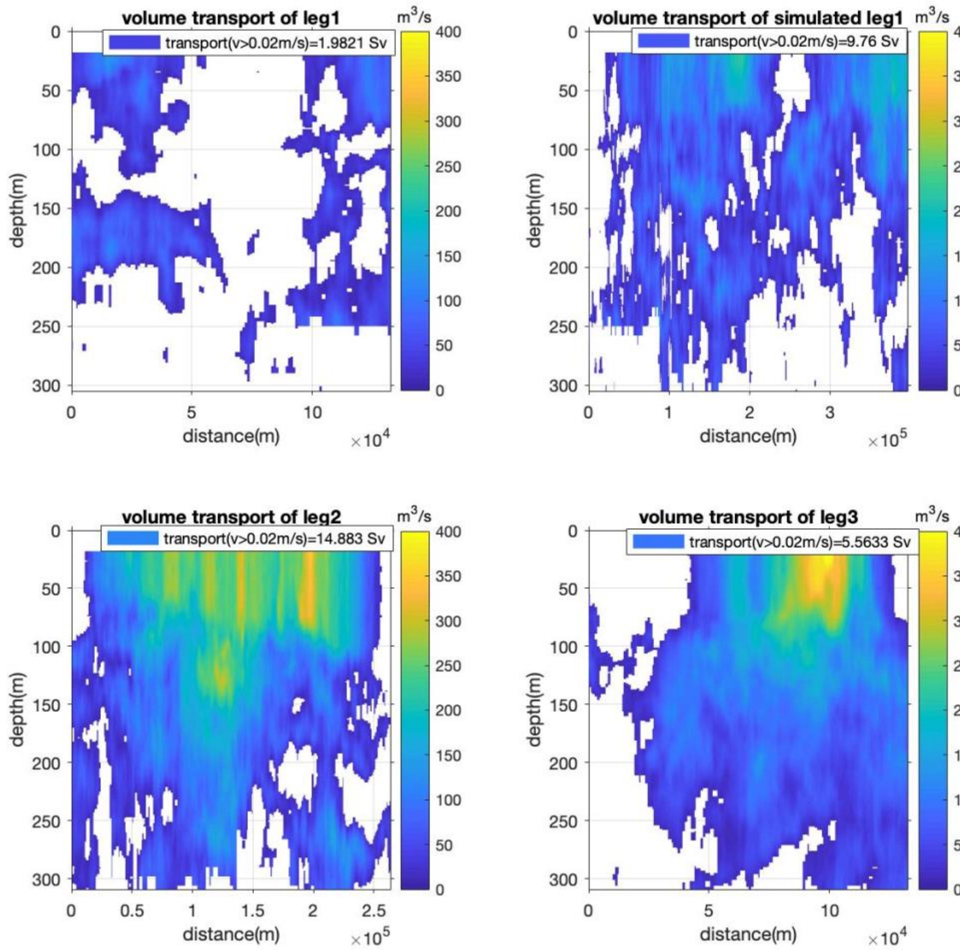

Figure 24. Volume transport of leg 1 (top left); volume transport of simulated leg 1 from14°S-18°S(top right); volume transport of leg 2 (bottom left); volume transport of leg 3 (bottom right). White space indicates that the along-stream velocity is less than 0.02 ms^{-1} and is therefore outside the EGC.

Figure 24 shows volume transport of leg 1, theoretic leg 1, leg 2, leg 3 at every grid point. Those patterns are similar to the velocity sections in each leg. Maximum volume transport is observed near the sea surface and the middle of each leg. The transport of each property across the three transects is shown in Table 3.

Table 3. Volume transport (Sv), heat transport(TW),salinity transport (kg/s), oxygen transport (umol/s) for the three transects. Only volume transport is available in the theoretic leg 1.

	Volume transport (Sverdrup)	heat transport (TW)	salinity transport (kg/s)	oxygen transport (umol/s)
leg1	2.0	3.9	$1.6\text{x}10^{9}$	$0.7\ \text{x}10^{10}$
Theoretic leg1	9.8	-	-	-
leg2	14.9	29.9	$12.1\ \text{x}10^{9}$	$5.8\ \text{x}10^{10}$
leg3	5.6	11.4	$4.6\ \text{x}10^{9}$	$2.4\ \text{x}10^{10}$

Leg1 had lower transport than the other two legs due to not crossing the strongest part of the EGC. The volume transport of simulated leg 1 reflects the actual transport of the current. Transport in leg 2 is triple that of leg 3. This may be due to the extended distance of leg 2 compared to leg 3 and the stronger current intensity. The distance of current and strength of velocity are two crucial factors that affect the transport.

4.4 Annual change of the EGC

As physical and biological properties are delivered by the transport of the EGC, the intensity of the current can decide how much nutrient can be transported into the LC to support winter primary productivity.

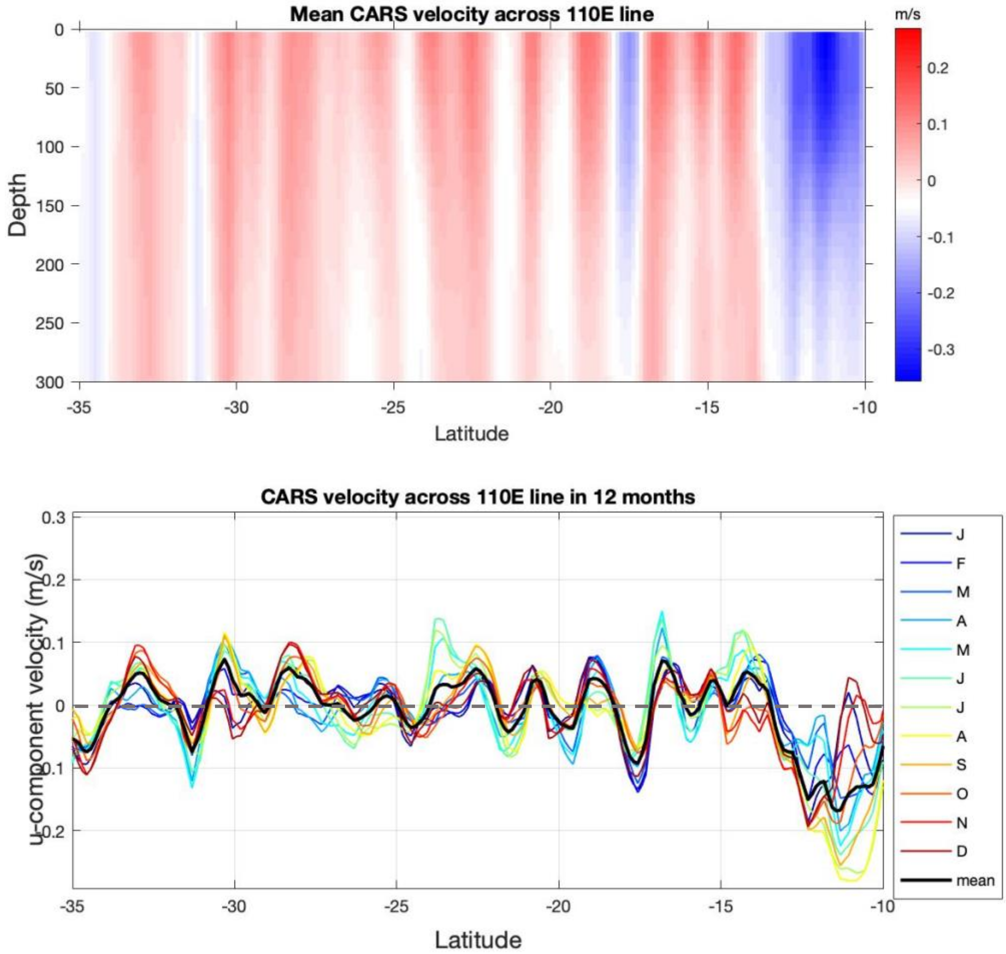

Figure 25. Annual mean velocity (eastward component) along 110 ° E line for twelve months from CARS (upper panel); seasonal variation of CARS velocity across 110 ° E line, each line presents the mean velocity of a month. The blue colors are for Jan, Feb, … and the colors change through to red in December. The solid black line is the annual mean velocity. The grey dashed line shows the 0m/s velocity.

The mean velocity field along the 110 ° E line from CARS and its variation throughout the year is shown in Figure 25. The vertical section of annual mean eastward velocity (Figure 25, top panel) shows mostly eastward flow (red shading) in the upper 300 m. These are the broad eastward flows that are made up of the EGC near 14°S-20°S and branches of the SICC further south (Menezes et al. 2013). The strong westward flow (blue shading) in the north is the South Equatorial Current. The narrow westward jet near 17°S -18 °S is likely to be an offshore meander of the EGC as we saw in the voyage Triaxus leg 2 sampled the EGC when it was flowing westward.

Figure 25, bottom panel shows the depth average current over the upper 300 m for each month from CARS. This figure indicates that the current across 110°E line is relatively stable. While there is a seasonal variation in the strength of each jet, there is not much seasonal variation in the position of each current jet. From Figure 25, the strongest current jet near 14°S-20°S shows up in May and June (Australia winter). The weakest current jet shows up in December and January which is Australian summer.

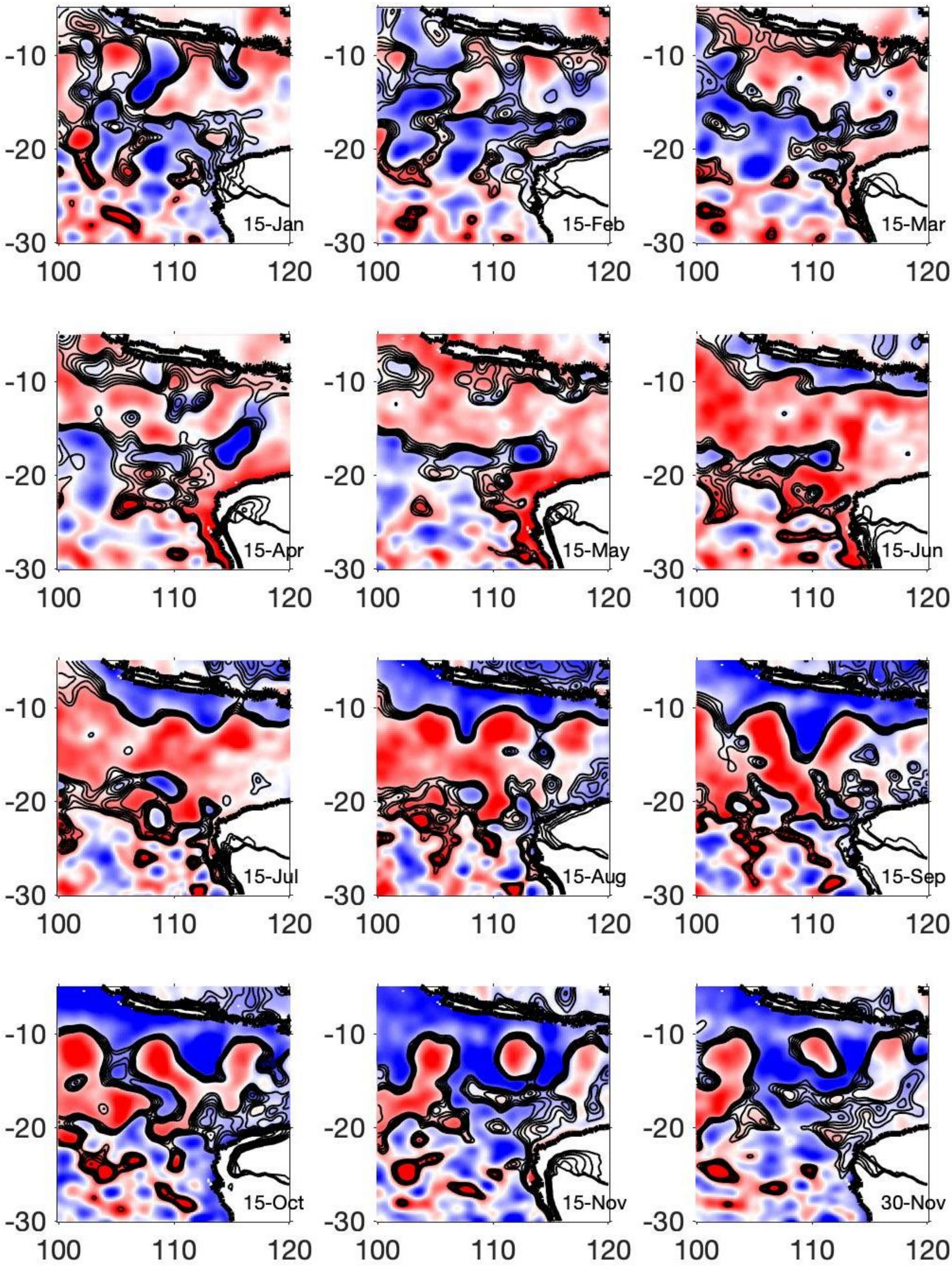

Figure 26. Sea surface height anomaly with surface velocity from satellite data for different months in 2019. The date is marked in the bottom right corner of every subplot. The black contours show the sea surface height and the grey quivers show the surface velocity. the SSH contours plotted range from minimum-value 2.34 mm to maximum-value 2.44 mm with an interval on 0.02mm. These contours highlight the path of the flow that joins the EGC. The

direction of current flow is such that the high sea surface height is to the left of the current. The red-blue color shows sea surface height anomaly with red color means higher than mean value and blue color means lower than mean value.

Figure 26 shows the position of the EGC and the variation in intensity thought the year (2019). It indicates that the area is rich in eddies. The eddies have a significant influence on the position and strength of the EGC, causing it to meander strongly as it approaches the Australian coastline. The strength of the EGC has seasonal variations, but there is no evidence of seasonal variation in the pathway (Figure 25 and 26). The main impact on the path of the EGC appears to be the eddy field.

5. Discussion

Interannual variation in 2019 year has been tested using the satellite data (Figure 26) which shows that the position and strength of EGC is basically stable but influenced by eddy events. Eddies in the LC have been explored in many studies (Waite et al. 2007). Conclusions from those studies describe the position and strength change of some eddies along the west coast of Australia. Those conclusions can also help to explain the variation of the EGC.

There are very few direct observations of the EGC so the annual and longer-period variations of the EGC are not well known. Menezes et al. (2013) used CARS and the Roemmich and Gilson gridded Argo Atlas (Roemmich & Gilson 2009) to show that the EGC has a maximum transport in May-June), corresponding to the time when the LC has its maximum transport (Furue et al. 2017). Our analysis of the satellite altimeter record in 2019 indicates the EGC is strongest in June when our measurements were made. It is meaningful to understand how the EGC changes annually so that we can learn about the annual change in nutrient amount that can be delivered into the LC. To estimate the annual variation of the EGC at the high-resolution of our observations, a longer period of observations that include nutrient measurements should be collected and examined in a later study. A numerical model that includes biogeochemistry could also be used to help this work. Future efforts could allow prediction of the strength of the EGC, and how much nutrient it is carrying, that would help forecast fishery production along west coast of Australia.

According to earlier studies (Ayers et al. 2014; Feng et al. 2003; Pearce & Phillips 1988), both the ITW and the LC are influenced by the El Nino-Southern Oscillation and Indian Ocean Dipole. Especially for the LC, the ENSO events have been verified to influence its strength as well as the productivity of the lobster fishery (ref to paper with figure in introduction showing lobster production versus El Nino index). Similarly, how the EGC changes in response to El Nino-Southern Oscillation and Indian Ocean Dipole should be studied in the future work. This can be examined using a model or the Argo data that is available since 2005.

In our project, a low oxygen layer can be observed clearly in the three transects across the EGC. It can be observed also in the CTD and CARS profiles along 110°E (Figure 13) at latitudes of about 10°-20°S. This is the latitude of the EGC according to the velocity profiles (Figure 14) and sea surface current from satellite (Figure 16). These figures provide evidence that the low oxygen layer exists in the depth range (100-200m) and that the EGC carries this layer westward to the west coast of Australia where it can enter the LC. The nitrate concentration is in this layer is inversely proportional to the oxygen concentration from examination of CARS and CTD data (Figure 15) and results from (Thompson, Wild-Allen, et al. 2011) (Figure 11). As a result, where there is a low dissolved oxygen layer, there also exists a high nitrate layer which combine to be the HNLDO layer.

As previously mentioned, the EGC is a retroflection circulation of the SEC which is known to contain high nitrate Indonesian tropical water from the ITF (Ayers et al. 2014). This provides evidence that the EGC is supplied with high nitrate water. However, it is still unclear if the HNLDO layer we observed in the EGC comes from the SEC and ITF.

The velocity profiles and transport of the EGC reveal that the EGC is delivering properties including water volume, heat, salt, oxygen and nitrate toward the LC. The HNLDO layer in the EGC is then a highly likely source of the HNLDO layer in the LC as well. From satellite figures (Figure 26), the path of the EGC into the LC is observed. The EGC has already proved to the one of the sources of volume transport into the LC from previous research (Furue et al. 2017). However, how the HNDLO layer is transported into the LC and how the layer is transported along the LC are not observed in our study. According to earlier work (Thompson, Wild-Allen, et al. 2011) (Figure 27), the layer appears to enter the LC at depth and enters the euphotic layer at ~ 31°S because of eddy activity. We need data further south of the three Triaxus tracks to verify the process of the entrance of the HNLDO layer into the LC. An earlier survey of the LC by *FRV Southern Surveyor* Voyage SS 04/2007 could provide this information. Analysis of this voyage data will be part of future work.

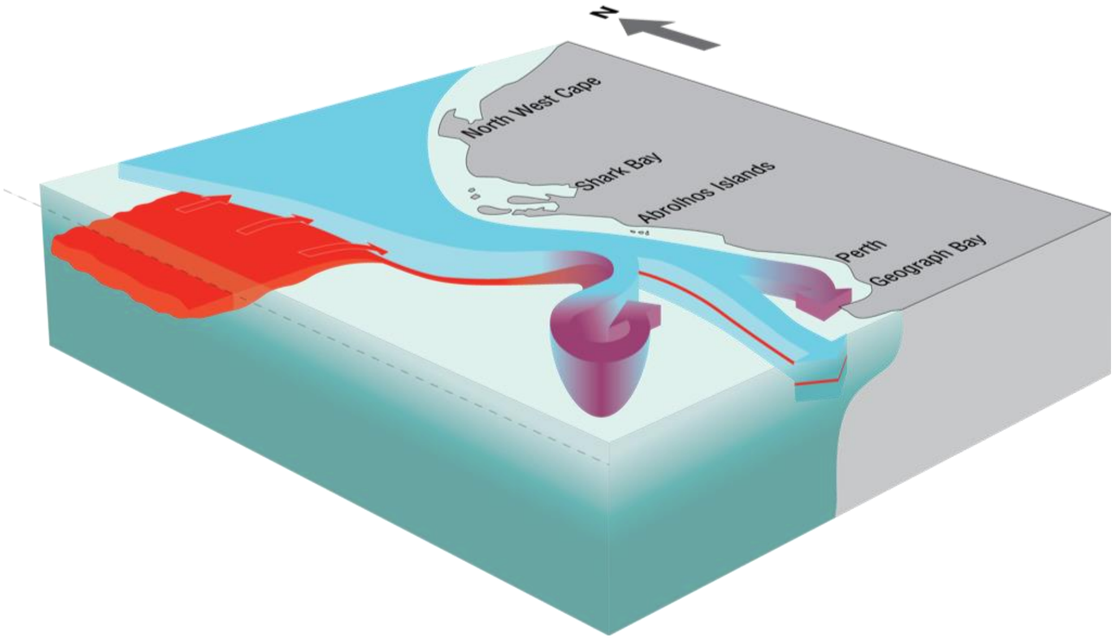

Figure 27. A conceptual representation of the strengthening Leeuwin Current (LC) and entrainment of thin layers of low dissolved oxygen (DO) and high nitrate concentrations as observed during late autumn 2007. At the latitudes of 22–25°S the LC is warmer and fresher than surrounding waters with strong vertical gradients in temperature, salinity, oxygen, fluorescence and nitrate observed between 50 and 80 m. Just below this there were thin layers of low DO and high nitrate (red color). The northern or western extent of these thin layers was not determined but they appear to be entrained into the LC at depth. Southwards

and near the Abrolhos Islands the Leeuwin Current narrows along the shelf edge, has cooled, and has high eddy kinetic energy. South of the Abrolhos Islands the LC produced a large warm core eddy observed off the shelf at ~31°S with relatively high nitrate (purple color) and low dissolved oxygen plus N:Si ratios all indicating the source of these waters to result from entrainment of this thin layer into the euphotic zone. Farther south, off Perth (~32°S), the LC existed in two modes. One mode with nitrate from this thin layer now mixed to the surface (purple color) and another with the thin layer still intact but at relatively shallow depths (~70 m). (Thompson, Wild-Allen, et al. 2011)

6 Conclusions

In this project, we described for the first time the water properties including velocity, temperature, salinity, oxygen and density in the EGC along three Triaxus transects that provide high spatial and temporal resolution and in supporting CTD data. The volume transport, heat transport, salinity transport and oxygen transport are all calculated at each Triaxus legs which indicate how much water volume, heat, salinity, oxygen, and nitrate is carried by the current. The seasonal change of the EGC position and strength was also explored using the CARS data along 110°E and the satellite sea surface height data in the area.

A persistent HNLDO layer was observed between 10°S-20°S in the 100-200m depth range of the EGC. We have shown that the layer is present in the EGC in all of Triaxus transects which get closer and closer to the LC. This suggests that the EGC provides the nitrate that supports the winter bloom in the LC. For larger scale, we found that the seasonal variation of the EGC is not obvious unlike the seasonal variation in the LC. The strength and position of the EGC is shown to be strongly influenced by the eddy activities.

The EGC is known to be one of the sources to the LC. Properties in the EGC were transported into LC at its north side, it brings relatively warm fresh tropical water and the HNLDO layer to the LC. Since the LC is important to the ecosystem and fisheries in the west coast of Australia (Lenanton et al. 1991; Rousseaux et al. 2012), it is important to figure out the source of nitrate that support the winter bloom. The offshore source of nitrate provide nitrate to the region where is considered lack of nutrient especially nitrate (Polovina, Howell & Abecassis 2008). As a result, the transport of the EGC is crucial for us to estimate the productivity in the LC and thus provide new knowledge to local fisheries.

For future study, the interannual variation of the EGC and the factors that influence it should be explored. It is also worthful to investigate how the HNLDO layer is modified as it enters the LC and moves southward along the coast.

7. References

Ayers, JM, Strutton, PG, Coles, VJ, Hood, RR & Matear, RJ 2014, 'Indonesian throughflow nutrient fluxes and their potential impact on Indian Ocean productivity', *Geophysical Research Letters*, vol. 41, no. 14, pp. 5060-5067.

Caputi, N & Brown, RS 1993, 'The effect of environment on puerulus settlement of the western rock lobster (PanuUrus cygnus) in Western Australia', *Fisheries Oceanography*, vol. 2, no. 1, pp. 1-10.

Caputi, N, Chubb, C, Melville-Smith, R, Pearce, A & Griffin, D 2003, 'Review of relationships between life history stages of the western rock lobster, Panulirus cygnus, in Western Australia', *Fisheries Research*, vol. 65, no. 1-3, pp. 47-61.

Caputi, N, Fletcher, WJ, Pearce, A & Chubb, CF 1996, 'Effect of the Leeuwin current on the recruitment of fish and invertebrates along the Western Australian coast', *Marine and Freshwater Research*, vol. 47, no. 2, pp. 147-155.

Collins, LB, Wyrwoll, KH & France, RE 1991, 'The Abrolhos carbonate platforms: geological evolution and Leeuwin current activity', *Journal - Royal Society of Western Australia*, vol. 74, pp. 47-57.

Condie, SA & Dunn, JR 2006, 'Seasonal characteristics of the surface mixed layer in the Australasian region: Implications for primary production regimes and biogeography', *Marine and Freshwater Research*, vol. 57, no. 6, pp. 569-590.

Cresswell, GR & Golding, TJ 1980, 'Observations of a south-flowing current in the southeastern Indian Ocean', *Deep Sea Research Part A, Oceanographic Research Papers*, vol. 27, no. 6, pp. 449-466.

Dietze, H, Matear, R & Moore, T 2009, 'Nutrient supply to anticyclonic meso-scale eddies off western Australia estimated with artificial tracers released in a circulation model', *Deep-Sea Research Part I: Oceanographic Research Papers*, vol. 56, no. 9, pp. 1440-1448.

Domingues, CM, Maltrud, ME, Wijffels, SE, Church, JA & Tomczak, M 2007, 'Simulated Lagrangian pathways between the Leeuwin Current System and the upper-ocean circulation of the southeast Indian Ocean', *Deep-Sea Research Part II: Topical Studies in Oceanography*, vol. 54, no. 8-10, pp. 797-817.

Doney, SC, Large, WG & Bryan, FO 1998, 'Surface ocean fluxes and water-mass transformation rates in the coupled NCAR climate system model', *Journal of Climate*, vol. 11, no. 6, pp. 1420-1441.

Fang, F & Morrow, R 2003, 'Evolution, movement and decay of warm-core Leeuwin Current eddies', *Deep-Sea Research Part II: Topical Studies in Oceanography*, vol. 50, no. 12-13, pp. 2245-2261.

Feng, M, Caputi, N, Penn, J, Slawinski, D, de Lestang, S, Weller, E & Pearce, A 2011, 'Ocean circulation, stokes drift, and connectivity of western rock lobster (Panulirus cygnus) population', *Canadian Journal of Fisheries and Aquatic Sciences*, vol. 68, no. 7, pp. 1182-1196.

Feng, M, Majewski, LJ, Fandry, CB & Waite, AM 2007, 'Characteristics of two counter-rotating eddies in the Leeuwin Current system off the Western Australian coast', *Deep-Sea Research Part II: Topical Studies in Oceanography*, vol. 54, no. 8-10, pp. 961-980.

Feng, M, Meyers, G, Pearce, A & Wijffels, S 2003, 'Annual and interannual variations of the Leeuwin Current at 32°S', *Journal of Geophysical Research C: Oceans*, vol. 108, no. 11, pp. 19-11.

Feng, M, Waite, AM & Thompson, PA 2009, 'Climate variability and ocean production in the Leeuwin Current system off the west coast of Western Australia', *Journal of the Royal Society of Western Australia*, vol. 92, no. 2, pp. 67-81.

Feng, M, Wijffels, S, Godfrey, S & Meyers, G 2005, 'Do eddies play a role in the momentum balance of the Leeuwin Current?', *Journal of Physical Oceanography*, vol. 35, no. 6, pp. 964-975.

Fieux, M, Molcard, R & Morrow, R 2005, 'Water properties and transport of the Leeuwin Current and Eddies off Western Australia', *Deep-Sea Research Part I: Oceanographic Research Papers*, vol. 52, no. 9, pp. 1617-1635.

Fletcher, WJ, Tregonning, RJ & Sant, GJ 1994, 'Interseasonal variation in the transport of pilchard eggs and larvae off southern Western Australia', *Marine Ecology Progress Series*, vol. 111, no. 3, pp. 209-224.

Furue, RYO, Guerreiro, K, Phillips, HE, McCreary, JP & Bindoff, NL 2017, 'On the leeuwin current system and its linkage to zonal flows in the south indian ocean as inferred from a gridded hydrography', *Journal of Physical Oceanography*, vol. 47, no. 3, pp. 583-602.

Godfrey, JS 1996, 'The effect of the Indonesian throughflow on ocean circulation and heat exchange with the atmosphere: A review', *Journal of Geophysical Research C: Oceans*, vol. 101, no. C5, pp. 12217-12237.

Godfrey, JS & Ridgway, KR 1985, 'The large-scale environment of the poleward-flowing Leeuwin Current, Western Australia: Longshore steric height gradients, wind stresses and geostrophic flow', *Journal of Physical Oceanography*, vol. 15, pp. 481-495.

Hanson, CE, Pattiaratchi, CB & Waite, AM 2005, 'Sporadic upwelling on a downwelling coast: Phytoplankton responses to spatially variable nutrient dynamics off the Gascoyne region of Western Australia', *Continental Shelf Research*, vol. 25, no. 12-13, pp. 1561-1582.

Hutchins, JB & Pearce, AF 1994, 'Influence of the Leeuwin Current on recruitment of tropical reef fishes at Rottnest Island, Western Australia', *Bulletin of Marine Science*, vol. 54, no. 1, pp. 245-255.

Joll, LM 1994, 'Unusually high recruitment in the Shark Bay saucer scallop (Amusium balloti) fishery', *Memoirs - Queensland Museum*, vol. 36, no. 2, pp. 261-267.

Lenanton, RC, Joll, L, Penn, J & Jones, K 1991, 'The influence of the Leeuwin Current on coastal fisheries of Western Australia', *Journal - Royal Society of Western Australia*, vol. 74, pp. 101-114.

Lluch-Belda, D, Crawford, RJM, Kawasaki, T, MacCall, AD, Parrish, RH, Schwartzlose, RA & Smith, PE 1989, 'World-wide fluctuations of sardine and anchovy stocks: The regime problem', *South African Journal of Marine Science*, vol. 8, no. 1, pp. 195-205.

Lourey, MJ, Dunn, JR & Waring, J 2006, 'A mixed-layer nutrient climatology of Leeuwin Current and Western Australian shelf waters: Seasonal nutrient dynamics and biomass', *Journal of Marine Systems*, vol. 59, no. 1-2, pp. 25-51.

Lourey, MJ, Thompson, PA, McLaughlin, MJ, Bonham, P & Feng, M 2013, 'Primary production and phytoplankton community structure during a winter shelf-scale phytoplankton bloom off Western Australia', *Marine Biology*, vol. 160, no. 2, pp. 355-369.

McDougall, TJ, Jackett, DR, Millero, FJ, Pawlowicz, R & Barker, PM 2012, 'A global algorithm for estimating Absolute Salinity', *Ocean Science*, vol. 8, no. 6, pp. 1123-1134.

Menezes, VV, Phillips, HE, Schiller, A, Bindoff, NL, Domingues, CM & Vianna, ML 2014, 'South Indian countercurrent and associated fronts', *Journal of Geophysical Research: Oceans*, vol. 119, no. 10, pp. 6763-6791.

Menezes, VV, Phillips, HE, Schiller, A, Domingues, CM & Bindoff, NL 2013, 'Salinity dominance on the Indian Ocean Eastern Gyral current', *Geophysical Research Letters*, vol. 40, no. 21, pp. 5716-5721.

Meyers, G, Bailey, RJ & Worby, AP 1995, 'Geostrophic transport of Indonesian throughflow', *Deep-Sea Research Part I*, vol. 42, no. 7, pp. 1163-1174.

Moore Ii, TS, Matear, RJ, Marra, J & Clementson, L 2007, 'Phytoplankton variability off the Western Australian Coast: Mesoscale eddies and their role in cross-shelf exchange', *Deep-Sea Research Part II: Topical Studies in Oceanography*, vol. 54, no. 8-10, pp. 943-960.

Paterson, HL, Feng, M, Waite, AM, Gomis, D, Beckley, LE, Holliday, D & Thompson, PA 2008, 'Physical and chemical signatures of a developing anticyclonic eddy in the Leeuwin Current, eastern Indian Ocean', *Journal of Geophysical Research: Oceans*, vol. 113, no. 7.

Pearce, AF & Phillips, BF 1988, 'Enso events, the leeuwin current, and larval recruitment of the western rock lobster', *ICES Journal of Marine Science*, vol. 45, no. 1, pp. 13-21.

Polovina, JJ, Howell, EA & Abecassis, M 2008, 'Ocean's least productive waters are expanding', *Geophysical Research Letters*, vol. 35, no. 3.

Roemmich, D & Gilson, J 2009, 'The 2004-2008 mean and annual cycle of temperature, salinity, and steric height in the global ocean from the Argo Program', *Progress in Oceanography*, vol. 82, no. 2, pp. 81-100.

Rossi, V, Feng, M, Pattiaratchi, C, Roughan, M & Waite, AM 2013, 'Linking synoptic forcing and local mesoscale processes with biological dynamics off Ningaloo Reef', *Journal of Geophysical Research: Oceans*, vol. 118, no. 3, pp. 1211-1225.

Rousseaux, CSG, Lowe, R, Feng, M, Waite, AM & Thompson, PA 2012, 'The role of the Leeuwin Current and mixed layer depth on the autumn phytoplankton bloom off Ningaloo Reef, Western Australia', *Continental Shelf Research*, vol. 32, pp. 22-35.

Schott, FA, Xie, SP & McCreary Jr, JP 2009, 'Indian ocean circulation and climate variability', *Reviews of Geophysics*, vol. 47, no. 1.

Smith, RL, Huyer, A, Godfrey, JS & Church, JA 1991, 'The Leeuwin Current off Western Australia, 1986-1987', *J. PHYSICAL OCEANOGRAPHY*, vol. 21, no. 2, pp. 323-345.

Sprintall, J, Wijffels, S, Chereskin, T & Bray, N 2002, 'The JADE and WOCE I10/IR6 Throughflow sections in the southeast Indian Ocean. Part 2: Velocity and transports', *Deep-Sea Research Part II: Topical Studies in Oceanography*, vol. 49, no. 7-8, pp. 1363-1389.

Stuart Godfrey, J & Weaver, AJ 1991, 'Is the Leeuwin Current driven by Pacific heating and winds?', *Progress in Oceanography*, vol. 27, no. 3-4, pp. 225-272.

Talley, LD & Sprintall, J 2005, 'Deep expression of the Indonesian Throughflow: Indonesian Intermediate Water in the South Equatorial Current', *Journal of Geophysical Research C: Oceans*, vol. 110, no. 10, pp. 1-30.

Thompson, PA, Bonham, P, Waite, AM, Clementson, LA, Cherukuru, N, Hassler, C & Doblin, MA 2011, 'Contrasting oceanographic conditions and phytoplankton communities on the east and west coasts of Australia', *Deep-Sea Research Part II: Topical Studies in Oceanography*, vol. 58, no. 5, pp. 645-663.

Thompson, PA, Wild-Allen, K, Lourey, M, Rousseaux, C, Waite, AM, Feng, M & Beckley, LE 2011, 'Nutrients in an oligotrophic boundary current: Evidence of a new role for the Leeuwin Current', *Progress in Oceanography*, vol. 91, no. 4, pp. 345-359.

Thompson, RORY 1984, 'Observations of the leeuwin current off Western Australia', *Journal of Physical Oceanography*, vol. 14, no. 3, pp. 623-628.

Waite, AM, Raes, E, Beckley, LE, Thompson, PA, Griffin, D, Saunders, M, Säwström, C, O'Rorke, R, Wang, M, Landrum, JP & Jeffs, A 2019, 'Production and ecosystem structure in cold-core vs. warm-core eddies: Implications for the zooplankton isoscape and rock lobster larvae', *Limnology and Oceanography*.

Waite, AM, Rossi, V, Roughan, M, Tilbrook, B, Thompson, PA, Feng, M, Wyatt, ASJ & Raes, EJ 2013, 'Formation and maintenance of high-nitrate, low pH layers in the eastern Indian Ocean and the role of nitrogen fixation', *Biogeosciences*, vol. 10, no. 8, pp. 5691-5702.

Waite, AM, Thompson, PA, Pesant, S, Feng, M, Beckley, LE, Domingues, CM, Gaughan, D, Hanson, CE, Holl, CM, Koslow, T, Meuleners, M, Montoya, JP, Moore, T, Muhling, BA, Paterson, H, Rennie, S, Strzelecki, J & Twomey, L 2007, 'The Leeuwin Current and its eddies: An introductory overview', *Deep-Sea Research Part II: Topical Studies in Oceanography*, vol. 54, no. 8-10, pp. 789-796.

Wijffels, S, Sprintall, J, Fieux, M & Bray, N 2002, 'The JADE and WOCE I10/IR6 Throughflow sections in the southeast indian ocean. Part 1: Water mass distribution and variability', *Deep-Sea Research Part II: Topical Studies in Oceanography*, vol. 49, no. 7-8, pp. 1341-1362.

Wilson, SG, Carleton, JH & Meekan, MG 2003, 'Spatial and temporal patterns in the distribution and abundance of macrozooplankton on the southern North West Shelf, Western Australia', *Estuarine, Coastal and Shelf Science*, vol. 56, no. 5-6, pp. 897-908.

Woo, M & Pattiaratchi, C 2008, 'Hydrography and water masses off the western Australian coast', *Deep-Sea Research Part I: Oceanographic Research Papers*, vol. 55, no. 9, pp. 1090-1104.

Zheng, S, Feng, M, Du, Y, Meng, X & Yu, W 2018, 'Interannual Variability of Eddy Kinetic Energy in the Subtropical Southeast Indian Ocean Associated With the El Niño-Southern Oscillation', *Journal of Geophysical Research: Oceans*, vol. 123, no. 2, pp. 1048-1061.

Appendix A

Table A4. Triaxus Configuration from IN2019_V03 Triaxus Data Processing Report that used for all Triaxus tows on voyage IN2019_V03

Sensor	Channel	SBE9 connector	Model	Serial	Cal. Date
CTD			SBE9+ V2	1312	20-Jul-2018
Primary Temperature		JB1	SBE3T	6302	03-Dec-2018
Primary Conductivity		JB2	SBE4C	4774	03-Dec-2018
Secondary Temperature		JB4	SBE3T	5932	12-Jan-2019
Secondary Conductivity		JB5	SBE4C	4773	07-Dec-2018
Primary Oxygen	A0	JT2	SBE43	3647	26-Nov-2018
Secondary Oxygen	A1	JT2	SBE43	3646	26-Nov-2018
PAR	A2	JT3	QCP2300HP	70562	01-Aug-2018
Eco Triplet	Payload 2		FLBBCD2K	4049	07-Sep-2018
Nitrate Sensor	Payload 3		Satlantic SUNA V2	449	
Optical Backscattering	Payload 4		SC6		
LOPC	Payload 7		Rolls Royce LOPC-1xT-3	11480	
Iridium Beacon	-	-	Xeos Apollo 3	132	

Table A5. CTD configuration from IN2019_V03 CTD Data Processing Report

Description	Sensor	Serial No.	A/D	Calibration Date	Calibration Source
Pressure	Digiquartz 410K-134	1312	P	20-Jul-2018	CSIRO
Primary Temperature	Sea-Bird SBE3T	6130	T0	12-Jan-2019	CSIRO
Secondary Temperature	Sea-Bird SBE3T	6180	T1	12-Jan-2019	CSIRO
Primary Conductivity	Sea-Bird SBE4C	4685	C0	14-Jan-2019	CSIRO
Secondary Conductivity	Sea-Bird SBE4C	4662	C1	14-Jan-2019	CSIRO
Primary Dissolved Oxygen	SBE43	1794	A0	30-Jul-2018	CSIRO
Secondary Dissolved Oxygen	SBE43	3198	A1	25-May-2018	Manufacturer
Fluorometer	Chelsea Aquatracka III	11-8206-01	A2	11-Dec-2018	Manufacturer
PAR	QCP – 2300 HP	70111	A3	1-Aug-2018	Manufacturer
LADCP Upward Facing	Teledyne 300kHz	16673	Internal	[Cal. Date]	[Cal. Source]
LADCP Downward Facing	Teledyne 150kHz	16710	Internal	[Cal. Date]	[Cal. Source]
UVP	Hydroptics UVP5	01721	A6/A7	[Cal. Date]	[Cal. Source]

Appendix B

Heat transport of Leg 1

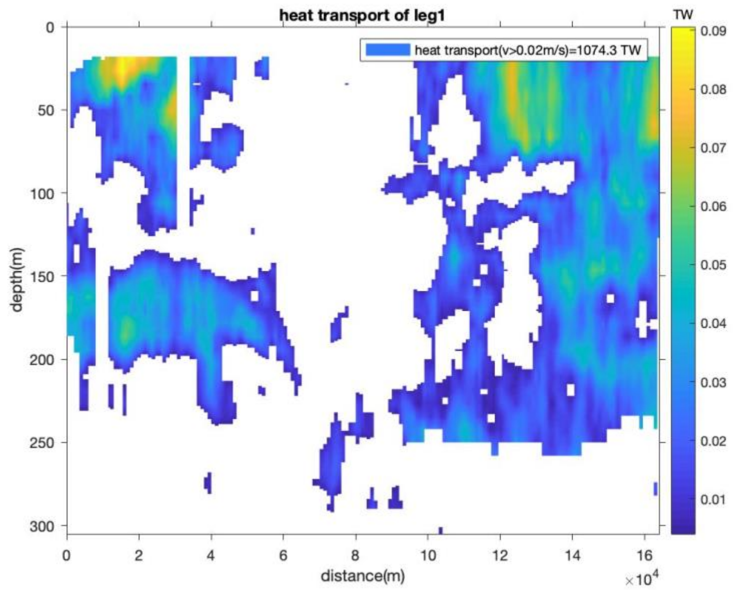

Figure B28. Heat transport of leg 1.

Heat transport of Leg 2

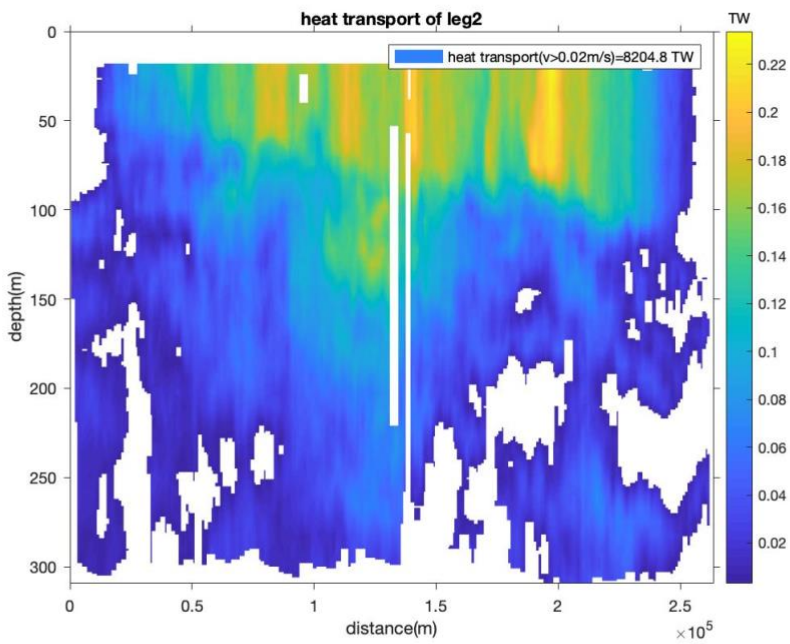

Figure B29. Heat transport of leg 2.

Heat transport of leg 3

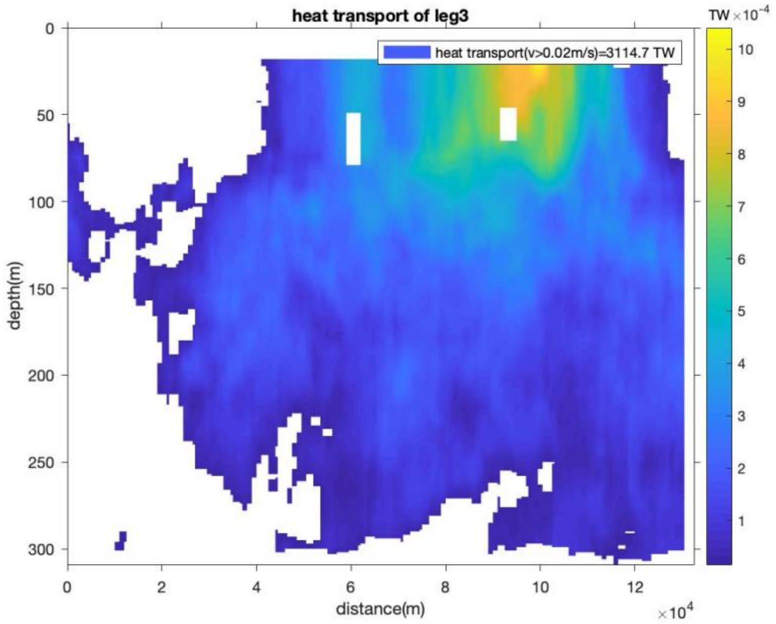

Figure B30. Heat transport of leg3

Salinity transport of leg 1

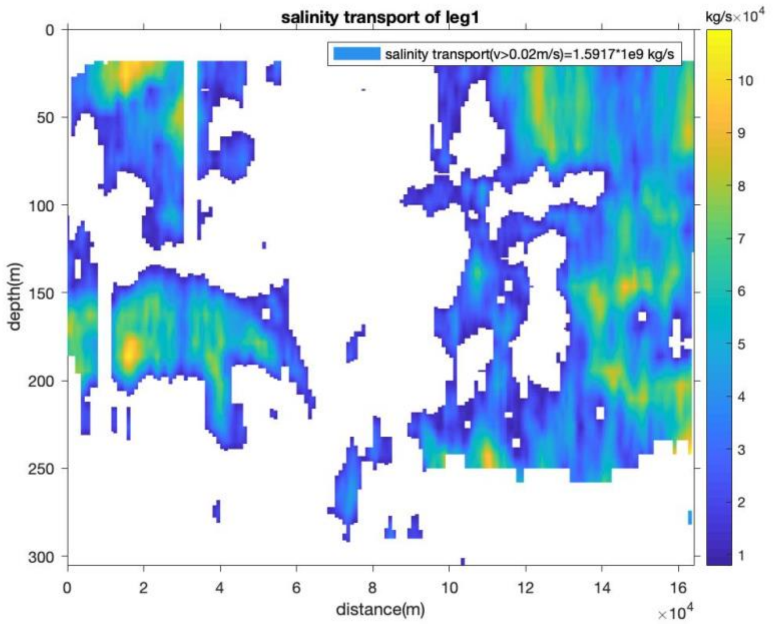

Figure B31. Salinity transport of leg 1.

Salinity transport of leg 2

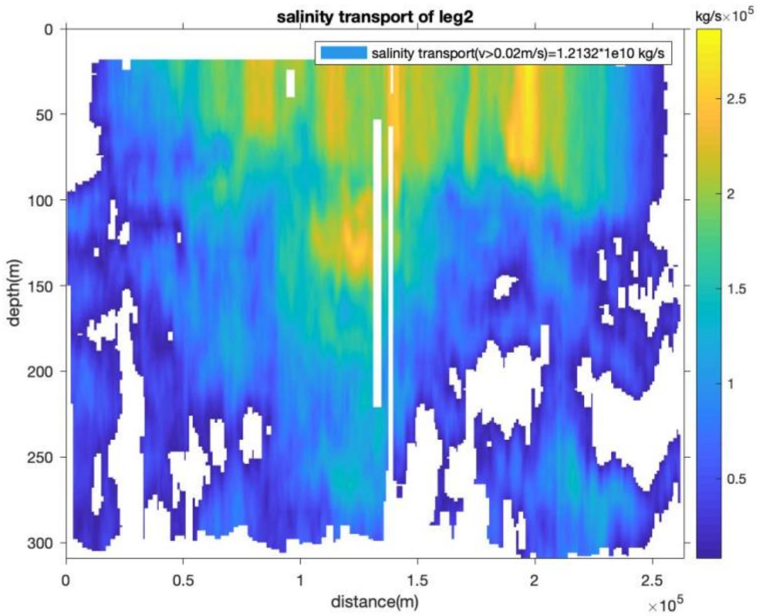

Figure B32. Salinity transport of leg 2.

Salinity transport of leg 3

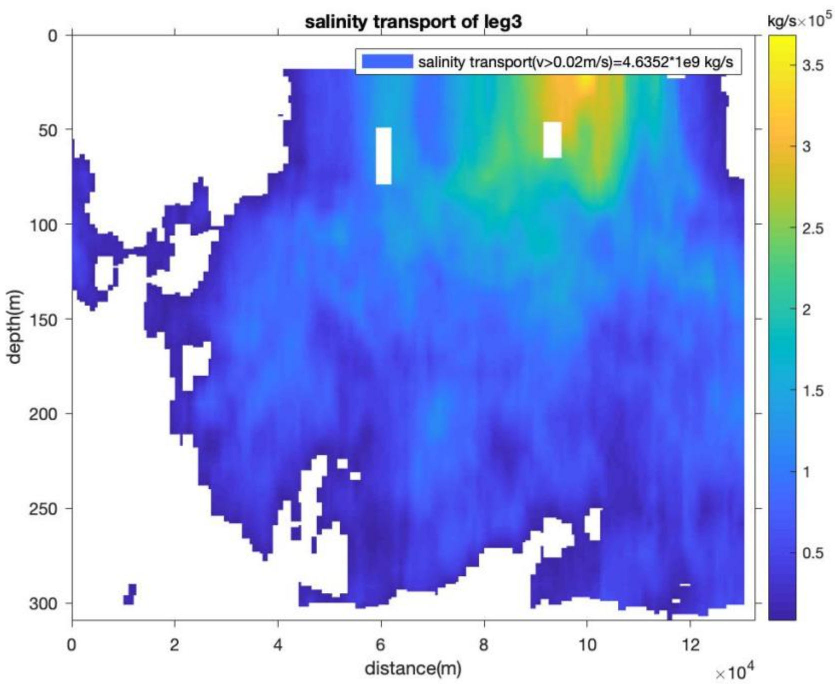

Figure B33. Salinity transport of leg 3.

Oxygen transport of leg 1

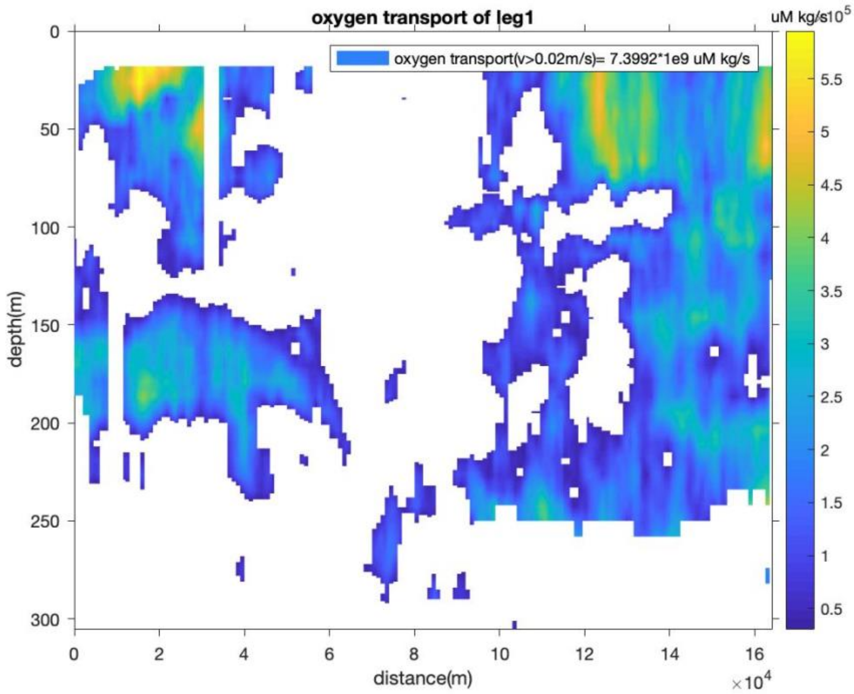

Figure B34. Oxygen transport of leg 1.

Oxygen transport of leg 2

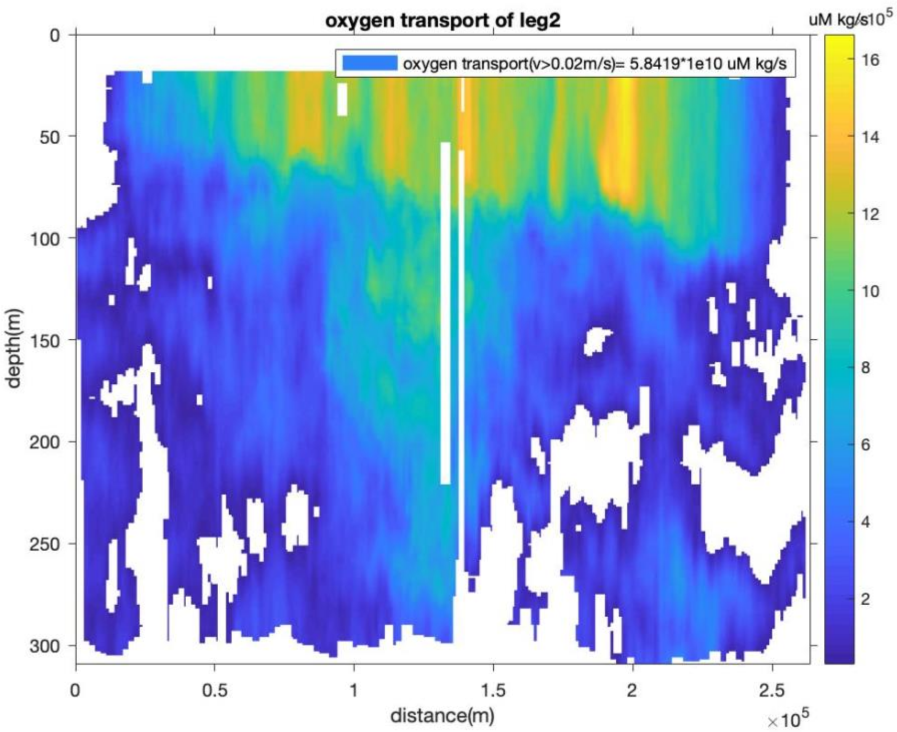

Figure B35. Oxygen transport of leg 2.

Oxygen transport of leg 3

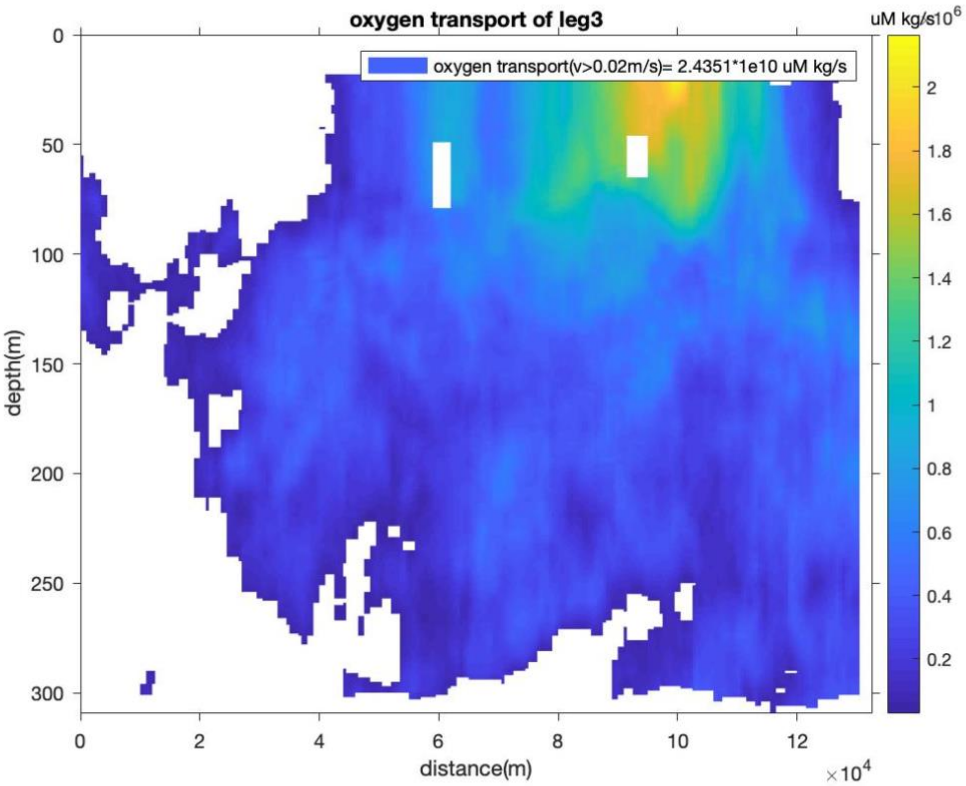

Figure B36. Oxygen transport of leg 3.

Appendix C

MATLAB function comp2speed

```
function [speed,dir] = comp2speed(u,v,rotation)

theta = zeros(size(u));
speed = zeros(size(u));
dir = zeros(size(u));

speed = sqrt(u.^2 + v.^2);

% Find the angle of the vector with respect to the transformed east
coord.
ind = find(u==0 & v>=0);
if(~isempty(ind))
   theta(ind) = 90*ones(size(ind));
end
ind = find(u==0 & v<0);
if(~isempty(ind))
   theta(ind) = 270*ones(size(ind));
end
ind = find(u~=0);
if(~isempty(ind))
   theta(ind) = atan(v(ind)./u(ind))*180/pi;
end

% Add 180 degrees to get direction right when u<0
ind = find(u<0);
theta(ind) = theta(ind)+180;

% Direction from True North
dir=90-theta+rotation;
ind=find(dir<0);
dir(ind)=dir(ind)+360;
end
```

MATLAB function speed2comp

```
function [u,v] = speed2comp(speed,dir,rotation)
```

```
theta=zeros(size(speed));
u=zeros(size(speed));
v=zeros(size(speed));

theta = 90-dir+rotation;
ind = find(theta<0);
theta(ind) = theta(ind)+360;

u = cos(theta*pi/180).*speed;
v = sin(theta*pi/180).*speed;
```